

Relating Patterns of Added and Redistributed Ocean Warming

EMILY NEWSOM,^a LAURE ZANNA,^a AND SAMAR KHATIWALA^b

^a *Courant Institute of Mathematical Sciences, New York University, New York, New York*

^b *Department of Earth Sciences, University of Oxford, Oxford, United Kingdom*

(Manuscript received 28 October 2021, in final form 3 March 2022)

ABSTRACT: Ocean warming patterns are a primary control on regional sea level rise and transient climate sensitivity. However, controls on these patterns in both observations and models are not fully understood, complicated as they are by their dependence on the “addition” of heat to the ocean’s interior along background ventilation pathways and on the “redistribution” of heat between regions by changing ocean dynamics. While many previous studies attribute heat redistribution to changes in high-latitude processes, here we propose that substantial heat redistribution is explained by the large-scale adjustment of the geostrophic flow to warming within the pycnocline. We explore this hypothesis in the University of Victoria Earth System Model, estimating added heat using the transport matrix method. We find that throughout the midlatitudes, subtropics, and tropics, patterns of added and redistributed heat in the model are strongly anticorrelated ($R \approx -0.75$). We argue that this occurs because changes in ocean currents, acting across pre-existing temperature gradients, redistribute heat away from regions of strong passive heat convergence. Over broad scales, this advective response can be estimated from changes in upper-ocean density alone using the thermal wind relation and is linked to an adjustment of the subtropical pycnocline. These results highlight a previously unappreciated relationship between added and redistributed heat and emphasize the role that subtropical and midlatitude dynamics play in setting patterns of ocean heat storage.

SIGNIFICANCE STATEMENT: The point of our study was to better understand the geographic pattern of ocean warming caused by human-driven climate change. Warming patterns are challenging to predict because they are sensitive both to how the ocean absorbs heat from the atmosphere and to how ocean currents change in response to increased emissions. We showed that these processes are not independent of one another: in many regions, changes in ocean currents reduce regional variations in the build-up of new heat absorbed from the atmosphere. This finding may help to constrain future projections of regional ocean warming, which matters because ocean warming patterns have a major influence on regional sea level rise, marine ecosystem degradation, and the rate of atmospheric warming.

KEYWORDS: Ocean; Subtropics; Ocean dynamics; Climate change; Climate models

1. Introduction

The great majority of human-driven excess heat in the climate system has been absorbed by the global oceans (Levitus et al. 2012; Roemmich et al. 2015; Cheng et al. 2017; Meysignac et al. 2019). The storage of this heat varies widely between ocean basins and depths (e.g., Zanna et al. 2019; Bronselaer and Zanna 2020; Bagnell and DeVries 2021; Frederikse et al. 2020; Cheng et al. 2017; Purkey et al. 2019), although uncertainty remains regarding the magnitude of regional changes (Cheng and Zhu 2015; Lyman and Johnson 2014; Wang et al. 2018). Model simulations agree that significant regional differences in ocean heat storage will persist into the future under continued CO₂ forcing, but they disagree on many details of these patterns, which vary across models and emission scenarios (Kuhlbrodt and Gregory 2012; Gregory et al. 2016; Todd et al. 2020; Dias et al. 2020; Couldrey et al. 2021; Frölicher et al. 2015; Ma et al. 2020). Uncertainty in both observed and projected ocean warming patterns stems, in part, from limitations in our

understanding of the physical processes shaping these patterns and their continued response to anthropogenic forcing. Reducing uncertainties in the pattern of ocean warming is a crucial prerequisite for accurate projections of regional sea level rise (Lowe and Gregory 2006; Todd et al. 2020; Couldrey et al. 2021) and changes in ocean biogeochemistry (Gruber 2011; Dunstan et al. 2018), as well as precipitation changes and atmospheric warming rates due to the influence of sea surface warming patterns on the hydrological cycle (Ma and Xie 2013; Zheng et al. 2016; Kent et al. 2015) and the transient climate sensitivity (e.g., Armour et al. 2013; Andrews et al. 2015; Dong et al. 2019). Hence, understanding the processes that set the pattern and magnitude of ocean warming is critical for robust and societally relevant projections of climate change over the next century.

A mechanistic understanding of ocean warming patterns is complicated by the number of processes involved, particularly since many are expected to change under anthropogenic forcing. Banks and Gregory (2006) pioneered a novel, now widely adopted, approach to this problem, which essentially poses this question: How much does anthropogenically driven ocean heat act like a passive tracer? To answer this question, they defined two distinct components of ocean warming. The first—“added heat” (sometimes termed “passive heat”)—is a hypothetical field representing all anomalous heat resulting from radiative

Supplemental information related to this paper is available at the Journals Online website: <https://doi.org/10.1175/JCLI-D-21-0827.s1>.

Corresponding author: Emily Newsom, ern275@nyu.edu

forcing taken at the ocean's surface and dispersed into the interior. The second—"redistributed heat"—encompasses all local ocean warming that occurs through the reorganization of preindustrial water masses by changes in ocean dynamics. The sum of these components describes the total ocean warming at a given location.

Separating added from redistributed heat in this manner is useful for several reasons. From a practical standpoint, the large-scale climatological circulation can be (relatively) constrained from observations, enabling direct estimates of added heat (e.g., Zanna et al. 2019; Bronselaer and Zanna 2020; Gebbie and Huybers 2019). Doing so in observations, as well as in models, helps identify the role of large-scale climatological ocean processes on global heat storage patterns. Indeed, many studies emphasize the importance of the background ocean state in setting key features of global ocean warming patterns (Church et al. 1991; Jackett et al. 2000), particularly the delayed warming of the Southern Ocean (Armour et al. 2016; Marshall et al. 2015; Frölicher et al. 2015; Marshall and Zanna 2014), the rate of heat uptake by the Atlantic meridional overturning circulation (AMOC) (Kostov et al. 2014) and Southern Ocean downwelling (Boé et al. 2009), and the increasing role of added heat in setting global heat storage patterns over time (Bronselaer and Zanna 2020).

Additionally, this decomposition helps quantify the impact that *changes* in ocean dynamics have on local warming rates. Many studies argue that redistributed heat has an equal or even greater effect on regional warming rates than the addition of new heat, particularly over the historical record (e.g., Bronselaer and Zanna 2020; Zika et al. 2021). Much of this work centers around high-latitude drivers. For instance, several modeling studies run with (Exarchou et al. 2015; Morrison et al. 2013) and without mesoscale eddy parameterizations (Gregory 2000) found that interior ocean warming was significantly enhanced by reduced high-latitude convection, and associated suppression of diffusive cooling via the Southern Ocean. Similarly, changes in the AMOC have been widely linked to heat redistribution both in the Atlantic (Xie and Vallis 2012; Winton et al. 2013; Rugenstein et al. 2013; Gregory et al. 2016; Garuba and Klinger 2016; Todd et al. 2020; Couldrey et al. 2021; Zanna et al. 2019; Marshall et al. 2015; Williams et al. 2021; Saenko et al. 2021) and globally through changes in interbasin exchange (Garuba and Klinger 2016; Sun 2020). Relatively fewer studies focus on drivers of heat redistribution outside of the high latitudes, despite emerging evidence that changes in subtropical circulations (Winton et al. 2013; Garuba and Klinger 2016; Williams et al. 2021; Saenko et al. 2021) and eastern boundary currents (Dias et al. 2020; Exarchou et al. 2015) may play a significant, if not dominant, role in global heat redistribution.

While the decomposition of added and redistributed heat is a powerful conceptual framework for disentangling the drivers of ocean warming patterns, it also introduces some complexity in interpretation and has led to diverging conclusions about the importance of different regional processes. Furthermore, because this decomposition enables the independent analysis of each component—isolating, for example, the roles of mixing, advection, and eddies on the individual evolutions of added or redistributed heat (e.g., Todd et al. 2020; Dias et al.

2020; Banks and Gregory 2006; Xie and Vallis 2012; Couldrey et al. 2021)—it can be difficult to synthesize a coherent picture of how they coevolve. In this way, the decomposition perhaps imparts the impression that patterns of added and redistributed heat can be understood independently of one another. Most importantly, the larger motivation of this decomposition is to constrain *total* ocean warming. A crucial step toward this goal is determining how these components relate, particularly given the time scale–dependent roles of each in ongoing climate change (Bronselaer and Zanna 2020).

To address this, in this study we ask: Is there relationship between patterns of added and redistributed heat? This question is motivated by the shared characteristics in their spatial patterns, particularly throughout the tropics and subtropics, apparent in both observational estimates and simulations (Bronselaer and Zanna 2020; Garuba and Klinger 2016; Banks and Gregory 2006; Dias et al. 2020; Todd et al. 2020; Xie 2020). We hypothesize that large-scale similarities in these patterns arise, at least in part, from the coevolution of changes in temperature gradients and changes in velocity in regions dominated by geostrophic balance. We argue that covariation of these changes, which has been invoked to relate the effects of velocity and temperature on global surface heat flux patterns (Hu et al. 2020) and ocean variability (Buckley et al. 2015), causes changes in geostrophic flow that redistribute background ocean heat away from regions of strong passive warming.

To do so, we set out to show the following: 1) patterns of added and redistributed heat are strongly anticorrelated; 2) changes in velocity explain patterns of subtropical–tropical heat redistribution; 3) changes in velocity are geostrophically balanced with changes in temperature and density gradients in many regions; and finally 4) heat redistribution coevolves with the depth of the subtropical pycnocline. In the following sections, we investigate these in a future warming simulation in the UVic ESCM (described below). We describe the model and methods in section 2, present the results in section 3, and discuss their implications and our conclusions in section 4.

2. Model and methods

a. Model

Any potential relationship between added and redistributed heat under CO₂ forcing could, in reality, be obscured for decades by internal oceanic variability (e.g., Palmer et al. 2017; Cheng et al. 2018; Bronselaer and Zanna 2020). We therefore use a modeling framework that generates little internal variability relative to, for instance, CMIP models (Frankcombe et al. 2015): the University of Victoria Earth System Climate Model (UVic ESCM) v2.9, a coupled climate model of intermediate complexity (Weaver et al. 2001). While the UVic ESCM features a 3D ocean general circulation model with a horizontal resolution of 1.8° × 3.6° and 19 layers, it is coupled to dynamic–thermodynamic sea ice, one-layer atmospheric energy–moisture balance, and land surface models, and thus does not explicitly include the effects of wind stress variability or change on ocean variability (Eby et al. 2009).

Despite its simple atmospheric component, however, ventilation by the UVic model's ocean circulation compares well to a variety of present-day physical, chemical, and biogeochemical observations (see Muglia et al. 2018; Khatiwala et al. 2019) and thus provides an optimal framework to study added heat uptake (e.g., Newsom et al. 2020). Here we examine a previously conducted simulation (Khatiwala et al. 2018) in which the model is forced with historical forcing between 1765 and 2000, after which CO₂ forcing follows an RCP8.5 scenario. Note that while wind stresses in the UVic are prescribed, the model includes an optional dynamic feedback in which wind stress changes are calculated from sea surface temperature changes. Here we disable this feedback in order to isolate the ocean's response to thermodynamic flux changes, an approach similar to, for example, those of Luo et al. (2015, 2017), Gregory et al. (2016), Todd et al. (2020), and Larson et al. (2018).

b. Added and redistributed components of ocean warming

As introduced in section 1, numerous processes influence ocean warming patterns. Specifically, the change in temperature at a given location evolves as

$$\begin{aligned} \frac{\partial T'}{\partial t} = & \frac{F'}{\rho_0 c_p} - \bar{\mathbf{v}} \cdot \nabla T' - \mathbf{v}' \cdot \nabla \bar{T} - \mathbf{v}' \cdot \nabla T' + \nabla \cdot (\bar{\boldsymbol{\kappa}} \nabla T') \\ & + \nabla \cdot (\boldsymbol{\kappa}' \nabla \bar{T}) + \nabla \cdot (\boldsymbol{\kappa}' \nabla T'). \end{aligned} \quad (1)$$

Here, all primed quantities represent the anomaly in that quantity from its mean-state value, that is, its value during an assumed steady-state climate as represented by an overbar. Unless otherwise stated, we define mean-state values as their time averages during the first 40 years of the simulation. We refer to this period (1765–1805) as the “background” climate, an approximately steady period in which a negligible fraction (<0.3%) of the eventual ocean warming (by 2100) is realized. In Eq. (1), we have assumed incompressibility, \mathbf{v} is the three-dimensional residual velocity field (including the parameterized bolus component), T is the temperature field, F is a surface heat flux, $\boldsymbol{\kappa}$ is a diffusivity tensor (encompassing the effective diffusivities of parameterized diapycnal and isopycnal mixing and diffusion), and ρ_0 and c_p are a reference density and specific heat for seawater, respectively [see the online supplemental material for the derivation of Eq. (1)].

As discussed in section 1, any local temperature anomaly T' can be further decomposed into two conceptually distinct components (e.g., Banks and Gregory 2006). The first component—the “added” temperature T_A —describes the temperature change associated with the addition of new heat to the ocean and its transport into the interior. By definition, $\bar{T}_A = 0$ in the background state, so we drop the prime for compactness. Globally, T_A comprises all *net* ocean warming and heat uptake due to anthropogenic forcing (meaning that $\rho_0 c_p \int_{V_g} T_A dV = \int_{A_g} F' dA$, where V_g and A_g are the volume and surface area of the global ocean, respectively). Locally, however, T_A will differ from T' where changing ocean dynamics redistribute background heat (present in the ocean prior to forcing) between locations. The local “redistributed” temperature change, T_R , encompasses this effect, such that together, $T' = T_A + T_R$. By this definition, T_R is

also zero before forcing ($\bar{T}_R = 0$); unlike T_A , T_R sums to zero globally ($\rho_0 c_p \int_{V_g} T_R dV = 0$). Plugging these terms into Eq. (1) and regrouping, we isolate the evolution of T_A as

$$\frac{\partial T_A}{\partial t} = \frac{F'}{\rho_0 c_p} - \bar{\mathbf{v}} \cdot \nabla T_A - \mathbf{v}' \cdot \nabla T_A + \nabla \cdot (\bar{\boldsymbol{\kappa}} \nabla T_A) + \nabla \cdot (\boldsymbol{\kappa}' \nabla T_A), \quad (2)$$

leaving

$$\begin{aligned} \frac{\partial T_R}{\partial t} = & -\bar{\mathbf{v}} \cdot \nabla T_R - \mathbf{v}' \cdot \nabla \bar{T} - \mathbf{v}' \cdot \nabla T_R + \nabla \cdot (\bar{\boldsymbol{\kappa}} \nabla T_R) \\ & + \nabla \cdot (\boldsymbol{\kappa}' \nabla \bar{T}) + \nabla \cdot (\boldsymbol{\kappa}' \nabla T_R). \end{aligned} \quad (3)$$

An important aspect of our definition in Eq. (2) is that F' includes *all* anomalies in heat flux relative to the background state—any new heat added to the ocean. Surface flux anomalies do include, however, the effects of redistributed heat on surface fluxes, often called the “redistributive heat flux” (e.g., Garuba and Klinger 2016; Dias et al. 2020). These effects exist on the conceptual interface of added and redistributed heat, and partitioning them into a given budget is ultimately a semantic or methodological choice. For instance, redistributed heat fluxes are generally included in the redistributed heat budgets in Flux-Anomaly-Forced Model Intercomparison Project (FAFMIP) experiments (Gregory et al. 2016). The specifications of our framework, however, enable us to distill the underlying relationship between purely “anomalous/added” and “background” heat in the ocean. More importantly, the large-scale characteristics of our results are consistent across frameworks, including FAFMIP (e.g., Banks and Gregory 2006; Gregory et al. 2016; Coudrey et al. 2021; Dias et al. 2020).

c. Inferring added and redistributed heat

To estimate the added temperature anomaly, T_A [Eq. (2)], surface temperature anomalies are treated like passive tracers and ventilated into the interior using the model's time-evolving circulation. In practice, this calculation is performed using the transport matrix method (TMM) (Khatiwala et al. 2005; Khatiwala 2007, 2018), an efficient numerical scheme for “offline” ocean tracer simulation. In this method, the ocean model's circulation is encoded as transport matrices (TMs), sparse matrix representations of the model's advective-diffusive tracer transport scheme, including all parameterized subgrid-scale processes. Here, the time-varying SST anomaly, defined for this calculation only as $SST'(x, y, t) = SST(x, y, t) - SST(x, y, 1765)$, is imposed as a surface boundary condition that is propagated into the interior via the TMM [see Khatiwala 2007; e.g., their Eq. (3)]. Monthly-mean TMs for the transient UVic simulation used in this study were extracted by Khatiwala et al. (2018). Both the TMs and boundary conditions (also monthly mean) are linearly interpolated to the current time step before being applied. This boundary forcing will drive a field of interior added temperature anomalies $\tilde{T}_A(x, y, z, t)$, where the tilde specifies quantity calculated with the TMs. Importantly, these boundary conditions will encompass the effects of all anomalous surface heat flux, including those affected by

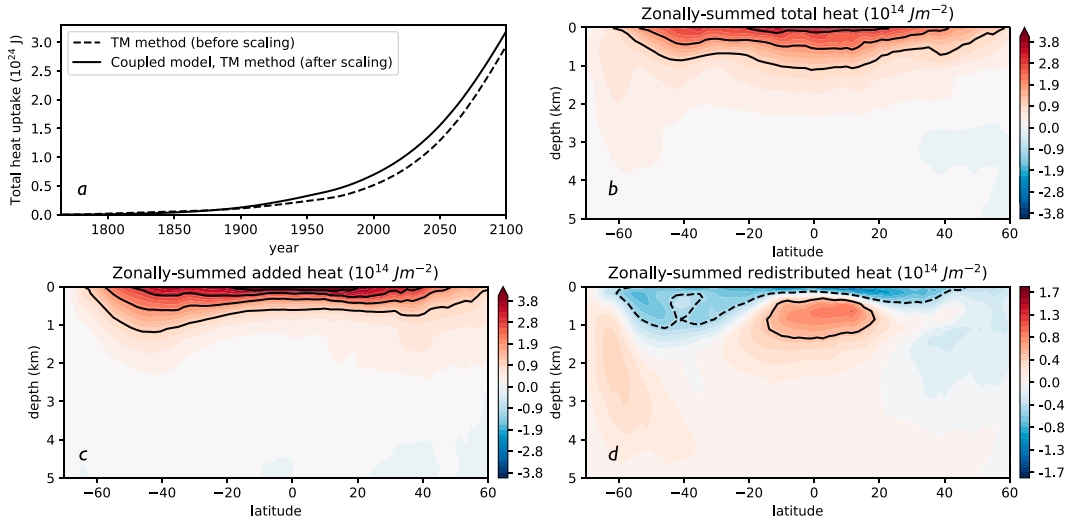


FIG. 1. Comparison of ocean heat uptake in the coupled UVic model and using transport matrices (TMs). (a) Total global ocean (volume V_g) heat uptake using the monthly mean TMs before scaling (i.e., $\rho_0 c_p \int_{V_g} \tilde{T}_A dV$, dashed) versus the total heat uptake in the UVic ESCM ($\rho_0 c_p \int_{V_g} T' dV$) and using scaled added temperature [$\rho_0 c_p \int_{V_g} T_A dV$; Eq. (4)], both represented by the solid black line. (b) Total anomalous ocean heat storage with depth and latitude in the UVic ESCM at year 2100 ($H_T = \rho_0 c_p \int_{X_g} T' dx$, where X_g is zonal ocean extent at each latitude). (c) As in (b), but for the added heat ($H_A = \rho_0 c_p \int_{X_g} T_A dx$). (d) As in (b) and (c), but for redistributed heat (i.e., $H_R = H_T - H_A$). Overlaid are black contours representing intervals of $1 \times 10^{14} \text{ J m}^{-1}$ in (b) and (c) and $5 \times 10^{13} \text{ J m}^{-1}$ in (d). See the online supplemental material for equivalent plots for unscaled fields.

circulation changes (the redistributed heat flux discussed above; e.g., Garuba and Klinger 2018), through their influence on SST'. In principle, $\tilde{T}_A(x, y, z, t)$ should thus encompass all interior warming that results from surface flux anomalies [and recover the quantity in Eq. (2); see the online supplemental material for more details]. As such, the global ocean heat content change, and thus the inferred global heat flux change, calculated using the TMs and the coupled UVic model should be equal. In practice, however, differences in the model's numerical advection scheme and that used for extracting the TMs can lead to small differences between frameworks (Khatiwala 2007; Kvale et al. 2017). Additionally, we do not capture covariance between ventilation and SST' on submonthly time scales. As a result, the TM method underestimates UVic by $\approx 9\%$ (Fig. 1a). By 2100, the TMM calculation implies a net heat uptake of 2770 ZJ, less than the 3050 ZJ in the UVic ESCM, although this difference is well within the spread of the CMIP5 and CMIP6 ensembles (e.g., Lyu et al. 2021).

To correct this discrepancy, though imperfectly, we scale \tilde{T}_A such that its global integral equals that of T' , where T' describes the local temperature anomaly in the UVic model, at all times:

$$T_A(x, y, z, t) = \tilde{T}_A(x, y, z, t) \times \left(\int_{V_g} T'(x, y, z, t) dV \bigg/ \int_{V_g} \tilde{T}_A(x, y, z, t) dV \right). \quad (4)$$

We use T_A in Eq. (4) as the “added temperature” in our analysis (i.e., all calculations and figures except Fig. 1a). From here, we can infer the redistributed temperature [Eq. (3)] as the residual of the T' and T_A : $T_R(x, y, z, t) = T'(x, y, z, t) - T_A(x, y, z, t)$ and ensure that this field sums to zero, globally. Comparison of results with and without the scaling are presented in the supplemental material (Figs. S1–S3). Note that, while simplistic, the scaling does not alter our main conclusions.

Finally, most of our results will compare the patterns of anomalous heat storage associated with different components of warming. We will use the terminology “added heat” (H_A), “redistributed heat” (H_R), and “total heat” (H_T) to describe heat content associated with T_A , T_R , and T' , respectively, which we mainly present in their vertical integrals:

$$H_A(x, y, t) = \rho_0 c_p \int_{-H}^{\eta} T_A(x, y, z, t) dz, \quad (5)$$

$$H_R(x, y, t) = \rho_0 c_p \int_{-H}^{\eta} T_R(x, y, z, t) dz, \quad (6)$$

$$H_T(x, y, t) = \rho_0 c_p \int_{-H}^{\eta} T'(x, y, z, t) dz, \quad (7)$$

where H is the ocean depth and η is the sea surface. The exception is Figs. 1c and 1d, which instead show zonal (not vertical) integrals of each component, respectively.

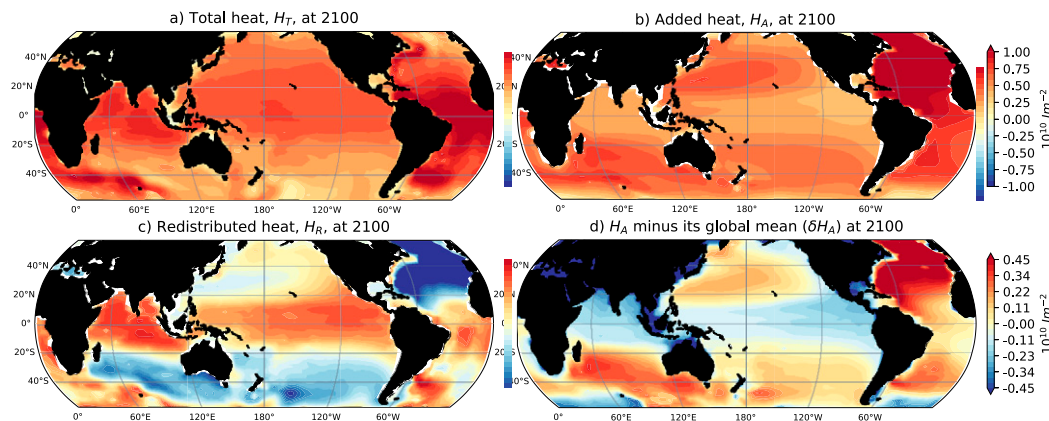


FIG. 2. Components of anomalous heat storage (year 2100) summed over the full depth of the ocean: (a) total heat uptake (H_T), (b) added heat (H_A), and (c) redistributed heat (H_R), which are all defined in Eqs. (5)–(7), and (d) δH_A (see text), which shows regions of greater or lesser H_A relative to its global mean value. Note that (a) and (b) share the same color bar, which differs from the color bar shared by (c) and (d).

3. Results

a. The relationship between added and redistributed heat

1) SPATIAL PATTERNS

We begin by examining the spatial distribution of anomalous ocean heat content at the end of the simulation. By 2100, the model's ocean has warmed significantly and with substantial regional variation, as illustrated in Fig. 2a, which sums the total anomalous heat storage over all depths [H_T ; Eq. (7)]. The majority of this heat ($\approx 81\%$) accumulates above 2000 m and equatorward of $\pm 60^\circ$ latitude (Fig. 1b), highlighting the importance of this region in storing the excess heat in the climate system.

Geographic variation in H_T arises from the large regional variation in both added heat H_A [Fig. 2b; Eq. (5)] and in redistributed heat H_R [Fig. 2c; Eq. (6)]. In its vertical sum, H_A accumulates primarily within the global midlatitudes and subtropics, by which we mean the region between roughly 50° and 15° latitude in both hemispheres. Relatively less is stored at lower or higher latitudes and, like H_T , the great majority of H_A resides in the upper ocean ($\approx 90\%$ above 2000 m, as is clear in Fig. 1c). The disproportionately strong subtropical accumulation of H_A is robust across estimates (e.g., Banks and Gregory 2006; Gregory et al. 2016; Garuba and Klinger 2016; Dias et al. 2020; Bronselaer and Zanna 2020; Todd et al. 2020) owing to the vigorous uptake and subsequent wind-driven subduction of heat from the midlatitudes of the Southern Ocean and subtropical gyre circulations in both hemispheres (Jackett and McDougall 1997; Armour et al. 2016; Frölicher et al. 2015; Zanna et al. 2019; Newsom et al. 2020). Together, these regions dominate the ventilation of the global subtropical pycnocline (e.g., Khatiwala et al. 2012; Luyten et al. 1983; Marshall and Speer 2012) and, accordingly, here more than 70% of the total global heat uptake occurs in the midlatitudes.

Heat redistribution (Fig. 2c) takes on a distinct spatial pattern, in part because, by construction, regions of positive

and negative H_R cancel, globally. Yet H_R opposes the pattern of H_A in many regions. Specifically, over the simulation, changes in ocean dynamics tend to move pre-existing heat out of the midlatitudes and subtropics and into the tropics, although this exchange differs in magnitude between ocean basins. This redistribution also mostly occurs within the upper ocean (Fig. 1d). As with H_A , the large-scale pattern of H_R , specifically the dipole in cooling and warming of the upper subtropical and tropical oceans (Figs. 1 and 2), is consistent with previous work (e.g., Banks and Gregory 2006; Gregory et al. 2016; Garuba and Klinger 2016; Dias et al. 2020; Bronselaer and Zanna 2020; Todd et al. 2020; Couldrey et al. 2021). The remainder of this study works to understand the drivers of the regional pattern of H_R and how it relates to H_A .

2) SPATIAL CORRELATION

While H_R and H_A arise from distinct mechanisms, their spatial patterns imply some interdependence. Over the course of the simulation, a strong anticorrelation emerges between H_A and H_R , as shown in Fig. 3a (calculated for the region between 50°S and 50°N and partitioned into basins). Their anticorrelation strengthens with time in all basins, exceeding $R \approx -0.7$ in the Indo-Pacific and $R \approx -0.83$ in the Atlantic, by 2100. The relationship between H_R and H_A captures the general tendency for adjustments in ocean dynamics to transport background heat away from regions where newly added heat accumulates the most (regions of high H_A) to the least (low H_A). We illustrate this phenomenon directly by subtracting the global average of H_A from its value at each point. This quantity, $\delta H_A(x, y) = H_A(x, y) - (1/A_g) \int_{A_g} H_A dA$, where A_g is the ocean surface area, is shown for 2100 in Fig. 2d. Throughout much of the ocean, H_R (Fig. 2c) and δH_A (Fig. 2d) are of opposite sign and comparable magnitude. Moreover, the temporal evolutions of H_R and δH_A are highly anticorrelated ($R < -0.9$) in many locations (Fig. 3b), particularly within the

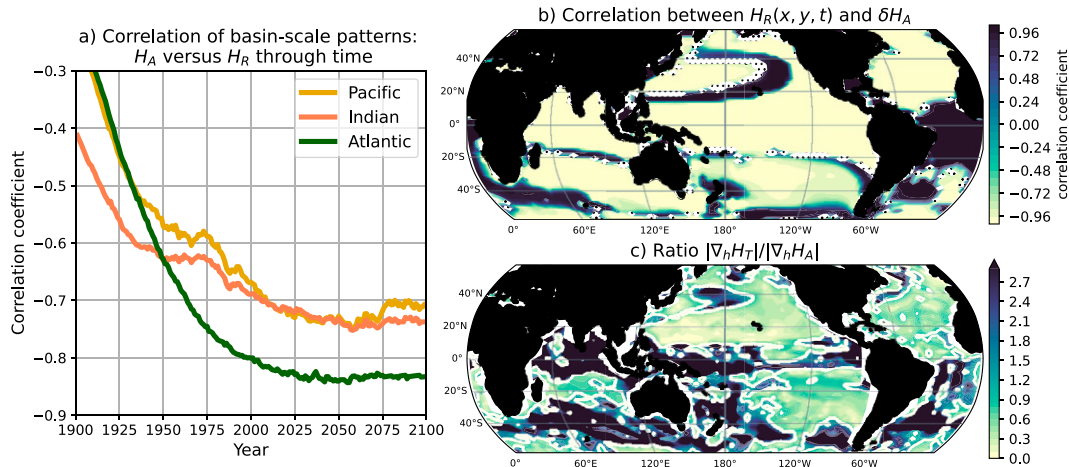


FIG. 3. The evolving relationship between added (H_A) and redistributed heat (H_R). (a) Correlation between spatial patterns (between 50°S and 50°N) of H_R and H_A for each year between 1900 and 2100 and partitioned into basins. Locations in which the absolute value $|H_R|$ equals or falls below 5% its global mean are not included in the calculation to avoid spuriously strong correlations. (b) Correlation between the time series of $H_R(x, y, t)$ and $\delta H_A(x, y, t)$ at each location between years 1900 and 2100. Regions in which $|H_R|$ falls below its 5% its global mean are masked (stippled areas). (c) Relative magnitude of the horizontal (subscript h) gradient in H_T vs H_A , or $|\nabla_h H_T|/|\nabla_h H_A|$, between $\pm 50^\circ$ and where $|\nabla_h H_T| = [(\partial H_T/\partial x)^2 + (\partial H_T/\partial y)^2]^{1/2}$ and $|\nabla_h H_A| = [(\partial H_A/\partial x)^2 + (\partial H_A/\partial y)^2]^{1/2}$. The light yellow in (c) denotes a ratio of one.

Indo-Pacific sectors. This relationship apparently breaks down in the tropical Atlantic, in which both H_R and δH_A grow over time and correlate positively. Because there is more added heat (per unit area) in the Atlantic, there local anticorrelation is more widespread if we instead compute δH_A by removing the basin-scale mean (i.e., a different constant), explaining why the basin-scale pattern correlation in Fig. 3a remains strong. Generally, however, Fig. 3b demonstrates that H_R concurrently opposes δH_A (at least over monthly time scales) across large swaths of the ocean. This process reduces the strong spatial gradients in heat storage that would otherwise develop if heat uptake were an entirely passive, unabated process. We quantified this effect with the ratio $|\nabla_h H_T|/|\nabla_h H_A|$ (Fig. 3c), where ∇_h denotes a horizontal gradient, which relates $|\nabla_h H_T| = [(\partial H_T/\partial x)^2 + (\partial H_T/\partial y)^2]^{1/2}$ and $|\nabla_h H_A| = [(\partial H_A/\partial x)^2 + (\partial H_A/\partial y)^2]^{1/2}$. Throughout most of the subtropics and into the tropics, $|\nabla_h H_T|$ is weaker than $|\nabla_h H_A|$ (i.e., $|\nabla_h H_T|/|\nabla_h H_A| < 1$; blue tones), demonstrating the large-scale smoothing effect of heat redistribution over these regions. Elsewhere—particularly near the equator where the Coriolis force is weak, and within western boundary currents where the momentum budget is more impacted by frictional terms (e.g., Luyten et al. 1983)—gradients are instead strengthened by heat redistribution.

b. Drivers of added and redistributed heat patterns

1) PARTITIONING OF HEAT CONVERGENCE

We now explore the mechanism relating H_A and H_R . As mentioned in section 1, a potential explanation for their coevolution (in Fig. 3) is the link between changes in spatial gradients in temperature and in geostrophically balanced flow. This link is assumed that 1) changes in advection

dominate heat redistribution between the subtropics and tropics, and 2) these changes are geostrophic. We test the first of these assumptions by using Eqs. (1)–(3) to quantify how changes in the residual velocity (i.e., including bolus terms) contribute to heat redistribution, relative to other processes. To do so, we integrate all terms vertically (full depth) and over the midlatitudes and subtropics (Figs. 4a,b; defined as the region within 50° – 15°N/S) and tropics (Figs. 4c,d; defined as $\leq 15^\circ\text{N/S}$). All fields are calculated from monthly mean values, and monthly anomalies in velocity and temperature are calculated by subtracting the mean seasonal cycle in the background state (years 1765–1805). Note that here mixing includes the anomalous heat convergence from parameterized diapycnal and isopycnal (Redi) mixing, background diffusivity, and convection (see Weaver et al. 2001), and is diagnosed as a residual from other terms in this analysis.

We begin by examining how changes in the residual velocity, acting across background temperature gradients [term $-\mathbf{v}' \cdot \nabla T$ in Eqs. (1) and (3)], redistribute heat between regions. As proposed, changes in velocity redistribute substantial quantities of background heat (more than 1000 ZJ by 2100) out of the midlatitudes and subtropics (solid teal line in Fig. 4a; see also Fig. S4a) into the tropics (Fig. 4b; see also Fig. S4b), $>97\%$ of which is driven by changes in horizontal velocity components. In fact, circulation changes are singularly responsible for the dipole-like structure of heat redistribution (i.e., Fig. 2c), since other dominant processes, like the mixing of redistributed temperature anomalies (Figs. S4a,b) and their transport by the background circulation (dashed green line in Figs. 4a,b and S4a,b), are of the opposite sign, with a larger impact in the tropics. Were heat redistribution driven by circulation changes alone, it would more than double.

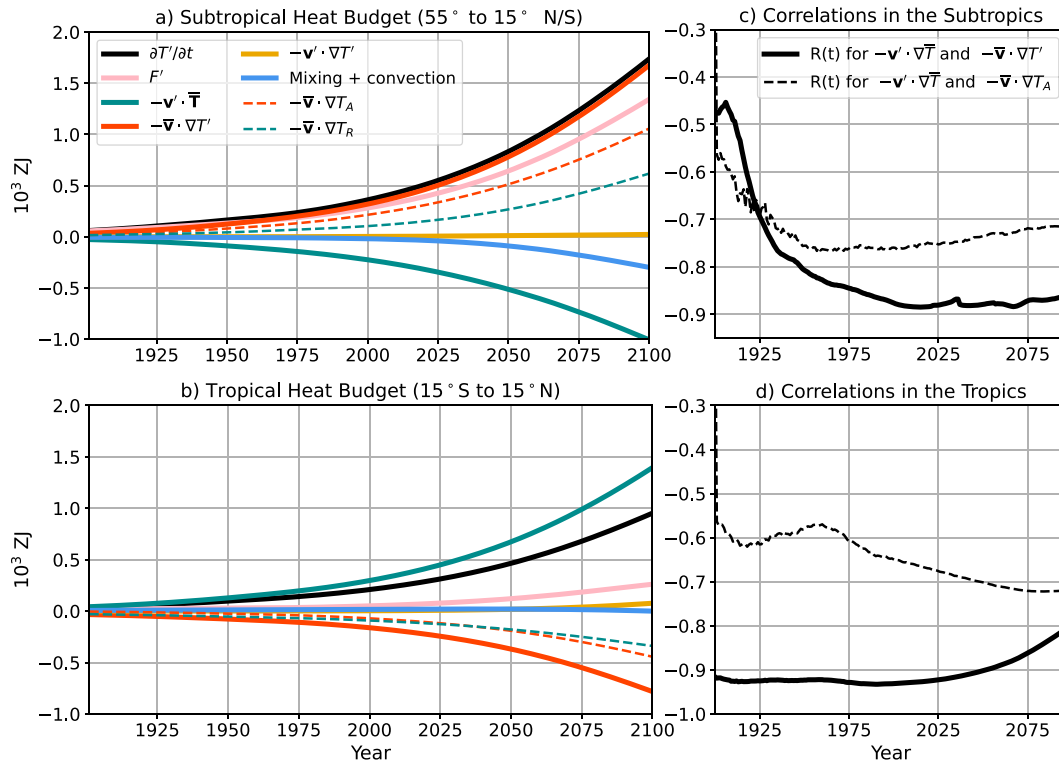


FIG. 4. Drivers of subtropical and tropical heat accumulation. Shown are regionally integrated cumulative anomalous heat flux convergence within (a) the global midlatitudes and subtropics (55° – 15° in each hemisphere) and (b) the global tropics (15° S– 15° N), over 1900–2100. All terms are defined in Eqs. (1)–(3) and are multiplied $\rho_0 c_p$. (c),(d) Correlation of patterns of $-\mathbf{v}' \cdot \nabla \bar{T}$ and $-\bar{\mathbf{v}} \cdot \nabla T'$ in the subtropics and tropics, respectively, represented by correlation coefficient $R(t)$, at each year between 1900 and 2100 (black solid). Note that in this calculation, all locations where the change in total advective heat flux at 2100 ($\approx -\mathbf{v}' \cdot \nabla \bar{T} - \bar{\mathbf{v}} \cdot \nabla T'$) falls below 5% of its background value (its time average during 1765–1805) is masked to avoid spuriously strong correlation. Also shown in (c) and (d) is the correlation between $-\mathbf{v}' \cdot \nabla \bar{T}$ and $-\bar{\mathbf{v}} \cdot \nabla T_A$ patterns (dashed line) in the subtropics and tropics, respectively. In this calculation, any region where either term's absolute value falls below 5% of its global mean value is masked.

The added heat pattern is dominated by a different balance. The strong subtropical accumulation of added heat is driven the significant influx of heat from the surface [≈ 1250 ZJ from term F' in Eqs. (1) and (2); pink line in Fig. 4a and Fig. S4c], and by the convergence of ≈ 1000 ZJ of added heat by the background flow [term $-\bar{\mathbf{v}} \cdot \nabla T_A$ in Eq. (2); dashed orange line in Fig. 4a and Fig. S4c]. The relatively weaker tropical added warming is sustained by positive surface fluxes and mixing of added temperature (Fig. 4b and Fig. S4d), although these effects are strongly offset by the divergence of T_A by the background flow (orange dashed line in Fig. 4b and Fig. S4d). In fact, while added heat is positive in both regions, its characteristic pattern—disproportionate accumulation within the subtropics relative to the tropics (Figs. 2b,d)—is primarily set by this background transport process ($-\bar{\mathbf{v}} \cdot \nabla T_A$), as it acts to diverge added heat from the tropics and into the subtropics. Absent this effect, added heat accumulation in the tropics and subtropics would be roughly equivalent (at ≈ 1000 ZJ).

Considering the T_A and T_R budgets in tandem reveals their effects on net warming (black line in Figs. 4a,b) and further clarifies the importance of the heat transport by the background

flow. Notably, mixing of added and redistributed temperatures, while nontrivial for each budget individually, nearly cancels in their regional sum (blue line in Figs. 4a,b). Net regional warming is thus dominated by a simpler balance, in which the background flow, acting across gradients of anomalous temperature ($-\bar{\mathbf{v}} \cdot \nabla T'$; solid orange line in Figs. 4a,b), largely opposes the circulation change–driven redistribution ($-\mathbf{v}' \cdot \nabla \bar{T}$; solid teal line in Figs. 4a,b; also discussed above). Net tropical warming results from the relatively smaller residual of the two (Fig. 4b), while their partial compensation in the subtropics enables intense regional surface warming to go nearly unopposed (Fig. 4a). The striking compensation between $-\bar{\mathbf{v}} \cdot \nabla T'$ and $-\mathbf{v}' \cdot \nabla \bar{T}$ has been emphasized previously (Hu et al. 2020; He et al. 2019; Marshall et al. 2015; Chen et al. 2019; Buckley et al. 2015; Williams et al. 2021) and holds not only at the regional scale (i.e., when integrated in Figs. 4a,b) but also locally in many places. Figures 4c and 4d show the correlation between monthly-mean patterns of vertically summed $-\bar{\mathbf{v}} \cdot \nabla T'$ and $-\mathbf{v}' \cdot \nabla \bar{T}$ in each basin for years 1900–2100 (solid black line), illustrating their strong local anticorrelation throughout most of the global midlatitudes and subtropics ($R \approx -0.87$ after 2000; Fig. 4c), as well as a lower latitudes,

where the correlation ranges from $R \approx -0.9$ to -0.8 between 2000 and 2100 (Fig. 4d).

This strong covariation between $-\bar{v} \cdot \nabla T'$ and $-\mathbf{v}' \cdot \nabla \bar{T}$ implies a physical linkage between them, which we return to in the following section. We first consider how such a linkage pertains to the relationship between H_A and H_R . Importantly, the term $-\bar{v} \cdot \nabla T'$ is influenced by both added and redistributed heat (because $T' = T_A + T_R$). However, gradients in added heat have a greater influence on its net regional effect: $-\bar{v} \cdot \nabla T_A$ exceeds $-\bar{v} \cdot \nabla T_R$ by 30% in the tropics and 75% in the subtropics (cf. the dashed orange and teal lines in Figs. 4a,b). Perhaps as a result, spatial patterns of $-\bar{v} \cdot \nabla T_A$ are themselves anticorrelated with the pattern $-\mathbf{v}' \cdot \nabla \bar{T}$ (Figs. 4c,d, dashed black line), which implies that the process strongly linking $-\bar{v} \cdot \nabla T'$ and $-\mathbf{v}' \cdot \nabla \bar{T}$ also results in the (albeit slightly weaker) correlation between $-\mathbf{v}' \cdot \nabla \bar{T}$ and $-\bar{v} \cdot \nabla T_A$. Hence, the terms dominant in setting added heat patterns are also locally anticorrelated with those dominating redistributed heat patterns, with a correlation coefficient similar to that relating H_R to H_A (the former exceeding $R = -0.7$, the latter around $R = -0.76$, on average between 50°N/S at 2100). This implies that the relationship between circulation changes and changes in temperature gradients are key to initiating, and reinforcing, the anticorrelation between H_A and H_R .

2) HOW “GEOSTROPHIC” IS HEAT REDISTRIBUTION?

We now test if the physical link between $-\mathbf{v}' \cdot \nabla \bar{T}$ and $-\bar{v} \cdot \nabla T'$ —implied by their strong anticorrelation and its impact on H_A and H_R patterns—is thermal wind balance. To do so we compare large-scale changes in horizontal (subscript h) velocity, \mathbf{v}'_h , to those that would arise were the flow in thermal wind balance with changes in horizontal temperature (more specifically, density) gradients. We call the latter the “thermal wind” velocity change, \mathbf{v}'_{tw} , with zonal (u'_{tw}) and meridional (v'_{tw}) components

$$u'_{tw}(x, y, z, t) = \frac{g}{\rho_0 f} \int_{z_0}^z \frac{\partial \rho'}{\partial y}(x, y, z, t) dz \quad \text{and}$$

$$v'_{tw}(x, y, z, t) = -\frac{g}{\rho_0 f} \int_{z_0}^z \frac{\partial \rho'}{\partial x}(x, y, z, t) dz. \quad (8)$$

Here, g is gravitational acceleration, ρ_0 is a reference density, and ρ' is the monthly potential density anomaly from the background seasonal climatology for all months between 1900 and 2100, both referenced to 2000 dB, and z_0 is a level of no motion in the ocean’s interior, here set to the total ocean depth. Regions within $\pm 6^\circ$ of the equator, where f becomes small, are masked in all calculations.

Reconstructed transport changes are compared to their “true” (coupled model) counterparts in Figs. 5a and 5d. Specifically, Fig. 5 compares the averaged change in residual zonal (Fig. 5a) and meridional (Fig. 5b) velocities between years 1900 and 2100 to the zonal (Fig. 5c) and meridional (Fig. 5d) thermal wind changes over the same years. All fields are summed over the top 2000 m and thus referred to as transports. Several aspects of Fig. 5 are noteworthy. First, throughout much of the subtropics and into the tropics, true transport

anomalies oppose the background circulation. Between around 30°–6°N/S, anomalous eastward flow (Fig. 5a) represents an average $\approx 15\%$ decrease, globally, in the west-flowing limbs of the subtropical gyres, relative to the background state. These changes are consistent both with the 5%–10% reduction in equatorward transport in the interior and eastern subtropics (between approximately 40° and 6°N/S; Fig. 5b) and with the robust spindown at depth of subtropical gyres across CMIP5 models under anthropogenic forcing (e.g., Wang et al. 2015; Garuba and Klinger 2018; Andrews et al. 2015; Luo et al. 2017; Li et al. 2019). At higher latitudes ($\approx 30^\circ$ – 50° N/S in Fig. 5a) swaths of intensified westward flow represent a poleward expansion of the subtropical circulations also noted in previous work (Yang et al. 2020), although the details differ regionally.

The second notable aspect of Fig. 5 is that the dominant circulation changes noted above are recovered by the thermal wind reconstructions (Figs. 5c,d). This implies that these broad-scale changes represent adjustments in the geostrophic flow, which here are largely driven by changes in temperature [and slightly damped by salinity changes; see our Fig. S5 and, e.g., Lowe and Gregory (2006), Todd et al. (2020), and Pardaens et al. (2011)]. Beyond these large-scale similarities, we note that reconstructed changes are significantly biased in some locations. For instance, thermal wind transports across the subtropical Pacific ($\approx 20^\circ$ – 30° N/S), are too far equatorward, such that zonal and meridional reconstructions are eightfold and sixfold too strong, respectively, and of the wrong sign across a narrow band in both hemispheres (cf. Figs. 5a,c). Similarly, equatorward of $\approx 8^\circ$ N/S and within eastern boundary regions, zonal reconstructions are nearly threefold (eastern Pacific) to sixfold (eastern and northern Atlantic) too strong and are generally collocated with equivalently biased meridional transport. Such dramatic errors mostly occur, however, where shared features of the model and reconstruction are misaligned—outside these locales, errors remain between 5% and 10%. Moreover, errors in these fields are expected toward the equator, where the Coriolis force is weak. Errors within boundary currents may stem from the complexity of frontal dynamics in these regions, further impacted by the coarseness of our model resolution (e.g., Ma et al. 2016).

Localized differences aside, the point is to demonstrate that changes in horizontal advection, which account for $>97\%$ of circulation change–driven heat redistribution from the subtropics and midlatitudes, are broadly related to adjustments in the geostrophic transport and balanced by anomalous temperature gradients. To illustrate this point directly, we compare the spatial distribution of horizontal heat convergence resulting from transport anomalies in Figs. 5a and 5b (i.e., $\mathbf{v}'_h \nabla_h \bar{T}$, integrated over the top 2000 m in Fig. 5d) to the heat convergence estimated from the equivalent thermal wind fields ($\mathbf{v}'_{tw} \nabla_h \bar{T}$ in Fig. 5f). As before, fields in Figs. 5e and 5f are not equal, with any differences in velocity amplified by strong local temperature gradients such that, in some regions, differences near an order of magnitude. Large local errors aside, the thermal wind reconstruction again captures the broad-scale pattern (and magnitude, in many regions) of Fig. 5e relatively well. Most notably, Fig. 5f recovers the heat divergence pattern out of the subtropical to midlatitude Pacific,

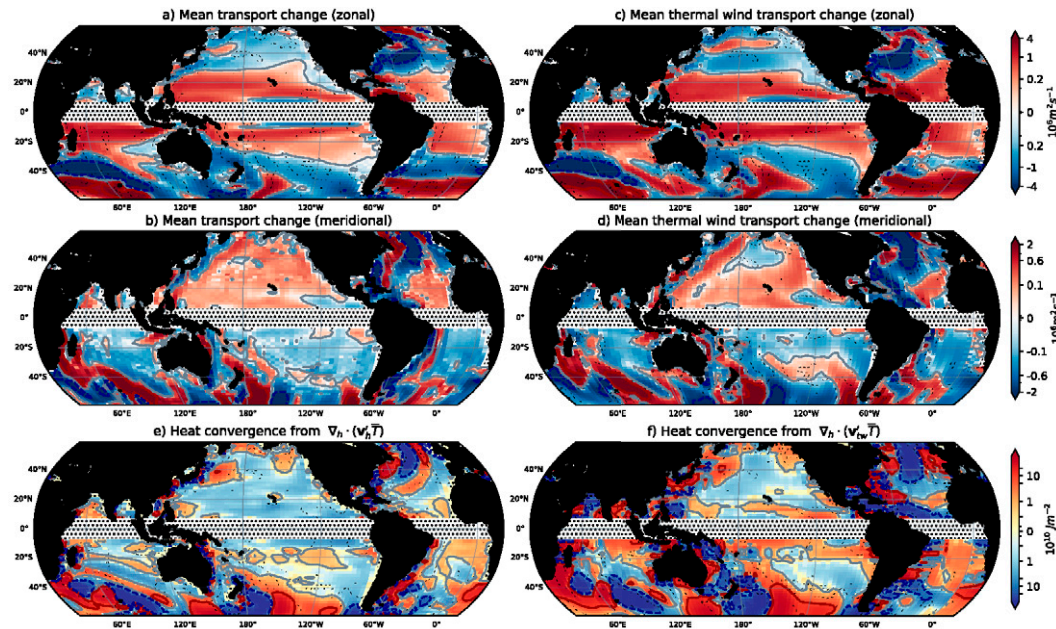


FIG. 5. Changes in geostrophic transport and heat convergence. (a) Time-averaged change in zonal residual velocity between years 1900–2100, integrated over the top 2000 m (thus referred to as a transport). (b) As in (a), but for the meridional residual transport. (c) As in (a), but for the zonal “thermal wind” velocity. (d) As in (b), but for the meridional thermal wind velocity. Both zonal and meridional thermal wind velocities are defined in Eq. (8). (e) Anomalous heat convergence in the upper 2000 m from changes in residual horizontal (subscript h) transports [i.e., (a) and (b)]. (f) As in (e), but for the anomalous heat convergence patterns estimated from the thermal wind velocities ($\nabla_h \cdot \mathbf{v}'_{tw} \bar{T}$) within the upper 2000 m. In all panels, the gray contour denotes regions of zero change. The red (positive) and blue (negative) contours denote regions of $\pm 5 \text{ m}^2 \text{ s}^{-1}$ in (a) and (c), $\pm 2 \text{ m}^2 \text{ s}^{-1}$ in (b) and (d), and $\pm 10^{10} \text{ J m}^{-2}$ in (e) and (f). Note that each row shares a color bar.

as well as the subtropical Indian and North Atlantic Oceans. Many features in the Southern Ocean are also captured relatively well by the reconstruction (both in location and magnitude), particularly throughout the Antarctic Circumpolar Current (ACC).

In summary, Figs. 5e and 5f suggest a key role for changes in geostrophic flow, balanced with ongoing changes in (primarily) ocean temperature, in heat redistribution out of the subtropics and midlatitudes. This argument sheds less light, however, onto dynamics in the tropics. One tentative explanation for the continued anticorrelation between H_A and H_R (Fig. 3) at low latitudes (masked in Fig. 5) is the connection between subtropical and tropical water mass pathways. The equatorial pycnocline is dominantly sourced from eastern subtropics, primarily from the Southern Hemisphere, as demonstrated by numerous Lagrangian tracer experiments (Fukumori et al. 2004; Qu et al. 2009, 2013; Nie et al. 2019). In that respect, subtropical flow—strongly constrained by geostrophy—may provide the boundary conditions for ageostrophic equatorial circulations. Conceivably, weakened equatorward flow in the eastern subtropics could reduce equatorial flow downstream. We leave this idea for future study, though we note that it is consistent with the dominance ($\approx 98\%$) of horizontal velocity changes in sustaining the circulation change–driven heat redistribution in the tropics (Figs. 4c,d), the flow changes generally opposed the background flow patterns (sustaining $\approx 10\%$

reduction in background horizontal heat divergence from the tropics). This idea also aligns with changes in the subtropical to tropical super-residual transport and heat convergence changes found in other studies (Dias et al. 2020; Luo et al. 2015).

3) RELATIONSHIP OF ADDED AND REDISTRIBUTED HEAT TO PYCNOCLINE DEPTH

Thus far we have shown diagnostically that the heat added to the ocean in response to CO_2 forcing is generally opposed by the redistribution of background heat content. The latter primarily occurs through the geostrophic adjustment in large-scale subtropical flow and reduces local gradients in warming. In light of these results, we now ask: Might we anticipate this redistributive response, and aspects of its spatial pattern, given the nature of added heat uptake and its relationship to the global pycnocline dynamics?

Specifically, as introduced in section 3a, the majority of added heat (H_A) in our experiment is taken up in the midlatitudes and stored between 60°N and 60°S and above the global pycnocline ($\approx 81\%$), here defined as the e -folding depth of the vertical potential density distribution (referenced to 2000 dB). This pattern highlights the key role midlatitude wind pumping plays both in propelling new heat into the interior (e.g., Armour et al. 2016; Frölicher et al. 2015) and in replenishing the global pycnocline (Khaliwala et al. 2012), thus maintaining

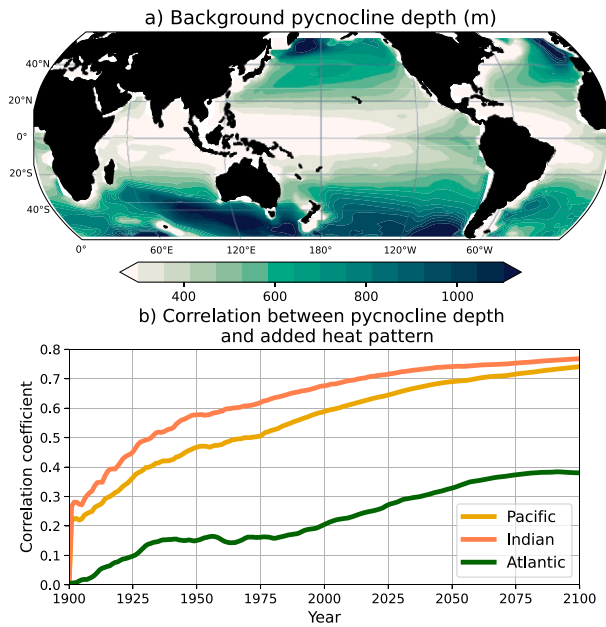


FIG. 6. Relationship between patterns of pycnocline-scale depth and added heat. (a) Distribution of background (average over first 40 years of simulation) pycnocline scale depth (m). (b) Correlation between added heat pattern and the pattern of background pycnocline depth between latitudes $+50^\circ$ and -50° for years between 1900 and 2100 and partitioned into the Pacific (gold), Indian (coral), and Atlantic (green) basins.

its depth (e.g., Gnanadesikan 1999) and spatial structure (e.g., Luyten et al. 1983). Further evidence of this connection is the resemblance between background pycnocline depth (Fig. 6a) and vertically integrated added heat (H_A in Fig. 2b) patterns. Similarities in these patterns—showing larger accumulation of H_A where the pycnocline is deep—is quantified by their strong correlation, which exceeds $R = 0.7$ in the Indo-Pacific after around year 2000 (Fig. 6b). In essence, the pycnocline restricts downward heat penetration such that new heat primarily accumulates above it.

How might we expect ocean dynamics to respond to pycnocline-intensified warming? A simple, reduced gravity (RG) perspective sheds light on this question. This framework, closely following Wang et al. (2015), reduces the ocean to an idealized Pacific-like basin of three layers: two dynamic upper layers separated from a stagnant abyssal layer by a “pycnocline” interface of depth h . The dynamic layers are ventilated by Ekman pumping, $w_e = -(\tau^x/f\rho_0)_y$, where f is the Coriolis parameter, ρ_0 is a reference density, subscript y denotes a meridional derivative, zonal wind stress τ^x varies only with latitude, the meridional wind stress is neglected, and interior flow (i.e., outside of frictional and Ekman layers and western boundary currents) is entirely geostrophic. Further details of the model are discussed in the online supplemental material (see also Wang et al. 2015; Luyten et al. 1983). In equilibrium, the divergence of geostrophic flow balances Ekman pumping, and h is given by

$$h(x, y) = \frac{1}{\Delta} \left[h_e^2 - \frac{2f^2}{g\alpha\beta(T_1 - T_2)} w_e (x_e - x) \right]^{1/2}. \quad (9)$$

Here, $\Delta = 1 + (\gamma + 1)(1 - ff_1)^2$, $\gamma = (T_1 - T_3)/(T_2 - T_3)$, β is the meridional derivative of f , h_e is the depth of the upper layer along the eastern boundary, x_e is the zonal distance across the basin, α is the coefficient of thermal expansion, T_1 , T_2 , and T_3 are the temperatures of the upper, middle, and abyssal layers, respectively ($T_1 > T_2 > T_3$), and we have assumed a linear, temperature-dependent equation of state. Pycnocline depth thus depends on the push and pull of the winds and the temperature difference between layers, which influences lateral pressure gradients and thus geostrophic flow. While simple, Eq. (9) captures both the magnitude and characteristic subtropical deepening of the pycnocline depth in, for example, the UVic model’s Pacific basin (Fig. 7b), when solved using the average values of all fields from UVic between 1765 and 1805 (the background pycnocline depth, h_0 , in Fig. 7a; see the supplemental material for details), implying that this dynamical balance establishes key aspects of pycnocline distribution. The pattern of vertically integrated added heat (H_A^{rg}) that would result from warming above h_0 (a zeroth-order approximation of added warming in UVic; see Fig. 1) can be estimated as $H_A^{\text{rg}} \approx \rho_0 c_p T_A^{\text{rg}} \times h_0$, where T_A^{rg} is the average added temperature anomaly [T_A ; Eqs. (2) and (4)] above the background pycnocline depth at 2100 in UVic. Though crude, H_A^{rg} (Fig. 7c) captures the magnitude and broad pattern of H_A in the UVic Pacific relatively well (Fig. 7d), again emphasizing that relationship between heat penetration and pycnocline depth.

Crucially, Eq. (9) also implies that, given no change in wind stress (as is the case in our simulation), the pycnocline depth must *adjust* to this warming due to its effect on lateral pressure gradients to remain in balance with Ekman pumping. Figure 7e shows this associated depth change (h'), which also includes the deepening of h_e associated with T_A^{rg} and illustrates that, under these dynamical approximations, a warming pycnocline shoals across the midlatitudes and subtropics and deepens at lower latitudes (Fig. 7e) in a pattern strongly anticorrelated to its background depth [$R = -0.87$, consistent with Wang et al. (2015)]. While more complex, similar characteristics emerge in the Pacific (Fig. 7f) between 43°N/S . There, like the RG model, pycnocline changes are strongly anticorrelated to the background state (at $R \approx -0.86$). The pycnocline shoals a maximum of 70 and 98 m in the Northern and Southern Hemispheres (NH and SH), respectively, approximately an $\approx 11\%$ reduction in maximum pycnocline depth in both regions, and deepens between 20° and 5°N/S , at maximum by 72 m (25%, although average regional changes are $\approx 9\%$). In comparison, the RG model predicts subtropical shoaling by $\approx 9\%$ (69 m; NH) and 12% (93 m; SH), and lower-latitude deepening (between 20° and 5°N/S) by 16% (a maximum 45 m).

The above exercise illustrates that the pycnocline must adjust to the accumulation of new heat above it, absent other forcing. Critically, this adjustment inherently redistributes heat because the upper ocean, even before forcing, contains more of the ocean’s heat than the abyss. The associated

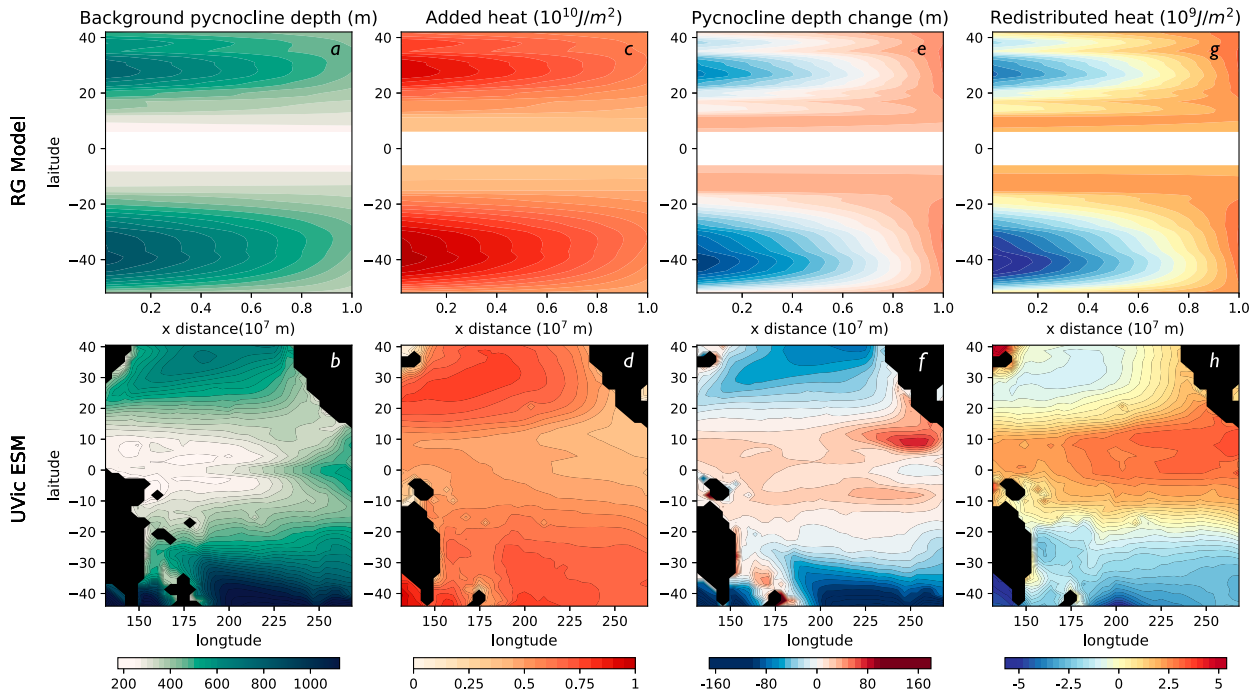


FIG. 7. Subtropical features in the reduced gravity model and UVic Pacific basin: (a),(b) the background pycnocline depth, (c),(d) the vertically integrated added heat at 2100, (e),(f) pycnocline depth change at 2100, and (g),(h) vertically integrated redistributed heat at 2100 for (top) the RG model and (bottom) UVic.

column-integrated heat redistribution, H_R^{fg} (Fig. 7g), can be approximated as $H_R^{fg} \approx \rho_0 c_p (T_P - T_3) \times h'$, where T_P is the average background temperature above h_0 . By construction, H_R^{fg} and H_A^{fg} will have the same relationship as h' and h_0 ($R = -0.89$), similar to H_R and H_A in UVic ($R \approx -0.71$ in the Pacific at 2100). As in other fields, H_R^{fg} misses key details of the H_R pattern in the UVic Pacific (Fig. 7f), particularly at the lower latitudes poorly represented by Eq. (9). However, broad correspondence between these patterns implies that the tendency for H_R to oppose H_A is tied to the adjustment of the pycnocline (i.e., its flattening) required to be by the added heat pattern itself.

How relevant is this implication outside the Pacific? Figure 8 compares global pycnocline depth changes (Fig. 8a) and redistribution patterns (Fig. 2c) in UVic between 50°N and 50°S. In the Indian Ocean, pycnocline changes resemble the Pacific and the RG model, shoaling a maximum 18% south of 18°S, and deepening by an average 13% north of 18°S. Clear differences emerge, however, in the Atlantic, particularly north of $\approx 35^\circ\text{N}$, where a strong dipole of pycnocline shoaling (by $\approx 25\%$) and deepening (by $\approx 30\%$) spans from east to west, a feature absent from the RG model and other basins. At lower Atlantic latitudes, the pycnocline deepens more than in other basins (by an average 20%) and extends farther poleward than other basins (shoaling occurs only south of around 34°S and in the eastern North Atlantic). This more complex pattern has been linked to local changes in air–sea fluxes and AMOC strength (Todd et al. 2020; Gregory et al. 2016; Bouttes et al. 2014) and their downstream effects (Zhai et al. 2014; Sun 2020), processes missing from our RG model and

discussed further in section 4. Regardless, the evolution of H_R is strongly correlated to pycnocline depth changes ($R > 0.9$) over broad swaths of all basins (Fig. 8b). The basin-scale uniformity of this relationship is reflected in the correlation between patterns of H_R versus pycnocline changes with time (Fig. 8c), which culminates at $R \approx 0.77$, 0.68, and 0.36 in the Pacific, Indian, and Atlantic basins. Interestingly, these relationships resemble the strength of (anti-)correlation between basinwide patterns of background pycnocline depth and depth changes, which also strengthens over this period to $R \approx -0.86$, -0.65 , and -0.31 in the Pacific, Indian, and Atlantic Oceans by 2100 (Fig. 8d). Together, global changes in Figs. 8b and 8d share elements of the RG representation, despite clear limitations of the latter. This implies that the relationship between H_R and H_A in many regions is mediated, in part, by the relationship between the pycnocline's background state and its changes (Wang et al. 2015) as it re-equilibrates to forcing (e.g., Zhai et al. 2014).

4. Discussion and conclusions

In this study, we explored drivers of ocean heat storage patterns in the UVic ESM (Weaver et al. 2001) under a high-emission (RCP8.5) anthropogenic forcing scenario. A primary result of our study is that patterns of ocean warming driven by anomalous heat uptake (added heat) are tightly linked to those due to changes in ocean circulation (redistributed heat) throughout most of the midlatitude, subtropical, and tropical oceans. While both added and redistributed heat patterns have been comprehensively studied (Banks and Gregory 2006; Xie

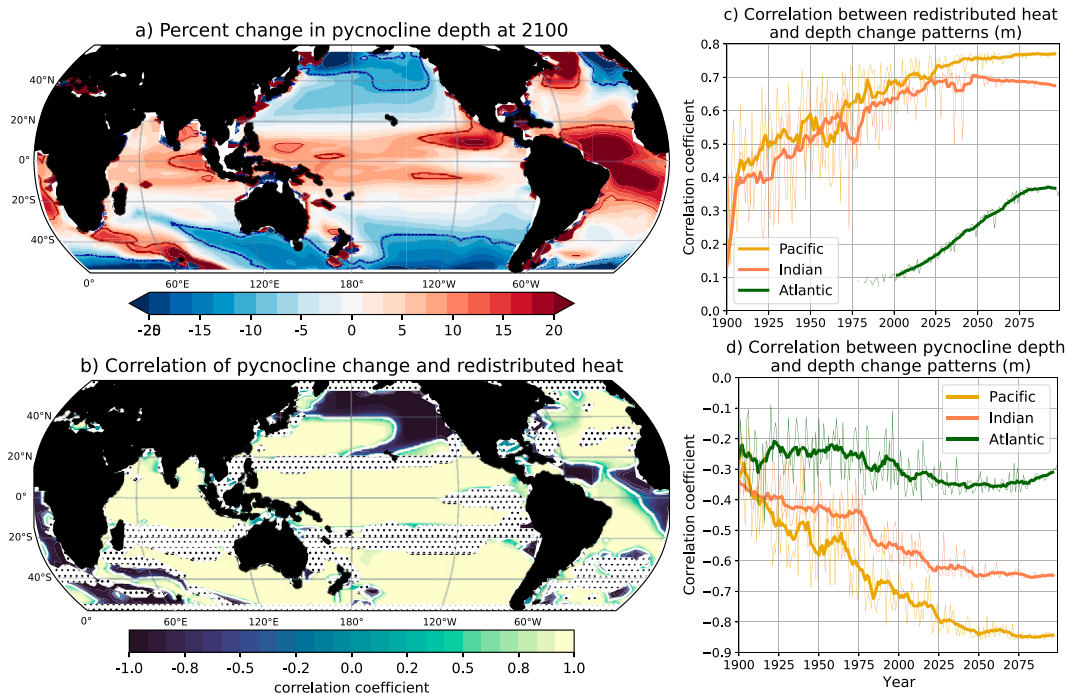


FIG. 8. Global-scale relationship between changes in pycnocline depth and redistributed heat. (a) Percent change in local pycnocline scale depth from the background state (Fig. 6), overlaid with contours of -10% (dark blue) and 10% (dark red) change. (b) Local correlation of the time evolution of vertically integrated redistributed heat $H_R(x, y, t)$ vs pycnocline depth changes between 1900 and 2100. Note that regions where the percent change in pycnocline depth [in (a)] is $\leq 5\%$ are masked (white stippled areas), and the white contour denotes zero correlation. (c) Correlation between basin-scale patterns of H_R and pycnocline depth changes between 50°N and 50°S for years 1900–2100. Note that in (c) monthly values (thin colored lines) are smoothed with a rolling-mean filter (window = 10 years; thick lines), locations where pycnocline depth changes are $\leq 5\%$ are masked [as in (b)], and only significant ($p < 0.01$) values are shown. (d) As in (c), but showing the correlation between background pycnocline depth and pycnocline depth changes [and only including locations where depth changes are $\leq 5\%$, as in (b) and (c)].

and Vallis 2012; Garuba and Klinger 2016; Banks and Gregory 2006; Garuba and Klinger 2018; Dias et al. 2020; Rugenstein et al. 2013; Bronselaer and Zanna 2020; Winton et al. 2013; Zanna et al. 2019; Lowe and Gregory 2006; Gregory et al. 2016; Todd et al. 2020; Bouttes et al. 2014; Williams et al. 2021; Saenko et al. 2021), their coupling has not been widely discussed. Here we demonstrated that their coevolution occurs, at least in part, because broad-scale changes in velocity are geostrophically balanced, or nearly so, with changes in temperature gradients. These circulation changes are the dominant driver of regional heat redistribution, consistent with previous work (e.g., Dias et al. 2020; Hu et al. 2020). We showed that over large scales, geostrophic heat redistribution tends to transport heat out of the subtropics and midlatitudes, where added heat storage is strong, and into the tropics, where added heat storage is relatively weak. As a result, total anomalous heat content is smoother throughout these regions than were the circulation unresponsive to forcing.

To highlight the role of geostrophy, we showed that large-scale patterns of circulation change–driven heat convergence can be reconstructed from changes in ocean density (largely controlled by temperature) using thermal wind. This correspondence is consistent with the strong anticorrelation ($R \approx -0.9$)

between anomalous heat convergence by background flow and flow changes. The strong anticorrelation between control circulation– and circulation change–induced heat convergence has been noted in multiple other frameworks (Marshall et al. 2015; He et al. 2019; Chen et al. 2019; Williams et al. 2021), several of which also invoke the ubiquity of thermal wind balance as its probable explanation (Hu et al. 2020; Buckley et al. 2015). In fact, Buckley et al. (2015) argue that these dual effects on heat convergence are so naturally linked that their separation is relatively meaningless in the context of climate variability. In contrast, in the climate warming scenario analyzed here, separating these processes is critical for understanding the divergent evolution of redistributed heat and added heat, since only the latter comprises the net ocean warming associated with anomalous ocean heat uptake (e.g., Banks and Gregory 2006).

We additionally proposed that elements of this oceanic response could be intuitively understood through the lens of global pycnocline dynamics. Specifically, in this study, more than 80% of added heat remains above the global pycnocline, consistent with previous work showing that anomalous heat content appears more uniform above fixed temperature surfaces than above fixed depths (e.g., Palmer and Haines

2009). Here, we further support this connection through the strong correlation, particularly in the Indo-Pacific, between geographic distributions of background pycnocline depth and column-integrated added heat—more heat is stored above a deeper pycnocline. This arguably occurs because the pycnocline restricts heat penetration and because its depth is set, in large part, by the same wind-driven ventilation (e.g., Gnanadesikan 1999; Khatiwala et al. 2012) that dominates ocean heat uptake (e.g., Armour et al. 2016; Frölicher et al. 2015; Shi et al. 2018). We demonstrate that this pycnocline-intensified warming, absent all other changes in the system, drives shoaling of the midlatitude and subtropical pycnocline (and its deepening at lower latitudes), in a conceptual model (Wang et al. 2015; Luyten et al. 1983). Arguably, an analogous effect of warming on dynamic sea level, absent in the conceptual model, could further amplify this response (e.g., Lowe and Gregory 2006). In fact, numerous processes missing from the simple model, among them changes in AMOC strength, wind stress, Southern Ocean eddies, and abyssal mixing, could alter pycnocline depth, perhaps even obscuring the effect of pycnocline warming (Gnanadesikan 1999; Nikurashin and Vallis 2012; Marshall et al. 2017; Saenko et al. 2018; Sun 2020). Notably, however, the subtropical pycnocline robustly shoals in our simulation, most clearly throughout the Pacific and Indian Oceans, consistent with the conceptual model as well as with CMIP5 models under increased CO₂ forcing (Wang et al. 2015). The key point is that pycnocline adjustment, regardless of its drivers, implicitly redistributes heat because waters above the pycnocline are generally warmer, even prior to forcing, than those below it. Throughout much of the UVic ocean, anomalies in pycnocline depth indeed correlate strongly ($R > 0.9$) with column-integrated redistributed heat. These relationships suggest that a component of global heat redistribution may be linked to a flattening global pycnocline under sustained anthropogenic heat uptake, a pattern which itself should oppose the pycnocline's background state and, thus, the distribution of added heat.

These broad conclusions are subject to several important caveats. The first is a clear distinction between the Atlantic and other ocean basins. Particularly, in the North Atlantic, heat redistribution is generally stronger and less directly related to pycnocline depth changes than throughout most of the Indo-Pacific. Differences in the Atlantic are perhaps unsurprising, given the substantial evidence that AMOC changes modulate basinwide and global heat storage patterns. Most canonically, the strong dipole in subpolar cooling and subtropical warming in the North Atlantic, evident in UVic, is widely attributed to changes in the AMOC and local air–sea fluxes (e.g., Bouttes et al. 2014; Huber and Zanna 2017) across numerous coupled climate (Winton et al. 2013; Gregory et al. 2016; Rugenstein et al. 2013; Couldrey et al. 2021; Menary and Wood 2018; Saenko et al. 2021) and ocean-only (Xie and Vallis 2012; Marshall et al. 2015; Todd et al. 2020) models. This effect is also apparent in observed ocean heat uptake and warming patterns (Zanna et al. 2019; Drijfhout et al. 2012) and consistent with the $\approx 30\%$ decrease in AMOC strength by 2100 in our simulation. In fact, AMOC changes can themselves induce regional opposition between added and redistributed heat patterns (Williams et al.

2021), which may explain their strong anticorrelation there. An AMOC slowdown could also modulate ocean heat storage in the Indo-Pacific (Garuba and Klinger 2018) through a far-field isopycnal response (Zhai et al. 2014; Sun 2020) and could involve more complex vertical structure than can be captured by our simple metric for pycnocline depth, as subtropical waters comprising the AMOC's upper branch deepen at the expense of its lower branch, (e.g., Xie and Vallis 2012; Winton et al. 2013; Sun 2020; Todd et al. 2020). A metric that better characterizes this structure (e.g., Feucher et al. 2019) might recover stronger a correlation between these fields in the North Atlantic and Southern Ocean, helping to might help disentangle the nuanced relationship between AMOC and pycnocline depth changes, apparent in simplified models (e.g., Zhai et al. 2014; Sun 2020).

However, as a counterpoint to this substantial historical emphasis on the AMOC and the high latitudes more generally (e.g., Gregory 2000; Boé et al. 2009; Morrison et al. 2013), our results suggest that subtropical ocean dynamics, and their response to anthropogenic forcing, may also play a central role in setting patterns of heat storage [as similarly emphasized by Dias et al. (2020), Garuba and Klinger (2016), Exarchou et al. (2015), Winton et al. (2013), and Williams et al. (2021)]. This conclusion is particularly clear in our somewhat simplified framework. The model used here generates minimal oceanic variability (Weaver et al. 2001), and we omit any forced change in wind stress. In reality and in more complex simulations, variability and wind changes could alter heat content at decadal time scales (e.g., Palmer et al. 2017; Tesdal and Abernathy 2021, among many others) and influence heat redistribution over time (Winton et al. 2013; Williams et al. 2021), complicating the response to thermohaline flux changes. Heat storage patterns might also be modified by the resolution of transient eddies and other small-scale ocean processes that are parameterized here. Regardless, we note that the broad spatial patterns of added and redistributed heat centered in our study are robust across a range of methodologies (Banks and Gregory 2006; Garuba and Klinger 2016, 2018; Dias et al. 2020; Bronselaer and Zanna 2020; Todd et al. 2020; Couldrey et al. 2021; Zika et al. 2021). This implies that the dynamics linking them discussed here may generally influence the ocean's response to climate warming, although this should be verified in more complex frameworks. From a practical standpoint, this linkage matters because estimating the distribution of added heat is (relatively) more straightforward to observe (Zanna et al. 2019; Gebbie and Huybers 2019; Bronselaer and Zanna 2020), and more robust across models (Todd et al. 2020; Couldrey et al. 2021), than observing or simulating the direct effect of circulation changes on heat storage. Hence, any component of heat redistribution that could be estimated from patterns of added heat storage—for instance, inferred as the “geostrophic” response to added heat—could be removed to better understand the additional effects of the AMOC, Southern Ocean processes, and many others. This separation could provide a pathway toward more robust projections of the ocean warming patterns, essential for reliable predictions of regional sea level rise over the coming century.

Acknowledgments. We thank three anonymous reviewers and our editor for their thoughtful comments, which

improved the manuscript. The authors also thank Jonathan Gregory for insightful discussion. This work was funded by the NERC Project NE/P019218/1 on Transient Tracer-Based Investigation of Circulation and Thermal Ocean Change (TICTOC) (E.N., L.Z., and S.K.) and the NSF OCE Grant 2048576 on Collaborative Research: Transient response of regional sea level to Antarctic ice shelf fluxes (E.N. and L.Z.). L.Z.'s work was also supported through the NERC Grant NE/R000727/1 (UKFAFMIP), and NSF OCE 2048576. S.K.'s work was additionally funded by U.K. NERC Grant NE/T009357/1. Computing resources were provided by the University of Oxford Advanced Research Computing (ARC) facility (<https://doi.org/10.5281/zenodo.22558>).

Data availability statement. Codes and further information about the transport matrices, and the simulation data used in this analysis, are publicly available at <https://doi.org/10.5281/zenodo.1246300>.

REFERENCES

- Andrews, T., J. M. Gregory, and M. J. Webb, 2015: The dependence of radiative forcing and feedback on evolving patterns of surface temperature change in climate models. *J. Climate*, **28**, 1630–1648, <https://doi.org/10.1175/JCLI-D-14-00545.1>.
- Armour, K. C., C. M. Bitz, and G. H. Roe, 2013: Time-varying climate sensitivity from regional feedbacks. *J. Climate*, **26**, 4518–4534, <https://doi.org/10.1175/JCLI-D-12-00544.1>.
- , J. Marshall, J. R. Scott, A. Donohoe, and E. R. Newsom, 2016: Southern Ocean warming delayed by circumpolar upwelling and equatorward transport. *Nat. Geosci.*, **9**, 549–554, <https://doi.org/10.1038/ngeo2731>.
- Bagnell, A., and T. DeVries, 2021: 20th century cooling of the deep ocean contributed to delayed acceleration of Earth's energy imbalance. *Nat. Commun.*, **12**, 4604, <https://doi.org/10.1038/s41467-021-24472-3>.
- Banks, H. T., and J. M. Gregory, 2006: Mechanisms of ocean heat uptake in a coupled climate model and the implications for tracer based predictions of ocean heat uptake. *Geophys. Res. Lett.*, **33**, L07608, <https://doi.org/10.1029/2005GL025352>.
- Boé, J., A. Hall, and X. Qu, 2009: Deep ocean heat uptake as a major source of spread in transient climate change simulations. *Geophys. Res. Lett.*, **36**, L22701, <https://doi.org/10.1029/2009GL040845>.
- Bouttes, N., J. M. Gregory, T. Kuhlbrodt, and R. S. Smith, 2014: The drivers of projected North Atlantic sea level change. *Climate Dyn.*, **43**, 1531–1544, <https://doi.org/10.1007/s00382-013-1973-8>.
- Bronselaer, B., and L. Zanna, 2020: Heat and carbon coupling reveals ocean warming due to circulation changes. *Nature*, **584**, 227–233, <https://doi.org/10.1038/s41586-020-2573-5>.
- Buckley, M. W., R. M. Ponte, G. Forget, and P. Heimbach, 2015: Determining the origins of advective heat transport convergence variability in the North Atlantic. *J. Climate*, **28**, 3943–3956, <https://doi.org/10.1175/JCLI-D-14-00579.1>.
- Chen, H., A. K. Morrison, C. O. Dufour, and J. L. Sarmiento, 2019: Deciphering patterns and drivers of heat and carbon storage in the Southern Ocean. *Geophys. Res. Lett.*, **46**, 3359–3367, <https://doi.org/10.1029/2018GL080961>.
- Cheng, L., and J. Zhu, 2015: Influences of the choice of climatology on ocean heat content estimation. *J. Atmos. Oceanic Technol.*, **32**, 388–394, <https://doi.org/10.1175/JTECH-D-14-00169.1>.
- , K. E. Trenberth, J. Fasullo, T. Boyer, J. Abraham, and J. Zhu, 2017: Improved estimates of ocean heat content from 1960 to 2015. *Sci. Adv.*, **3**, e1601545, <https://doi.org/10.1126/sciadv.1601545>.
- , G. Wang, J. P. Abraham, and G. Huang, 2018: Decadal ocean heat redistribution since the late 1990s and its association with key climate modes. *Climate*, **6**, 91, <https://doi.org/10.3390/cli6040091>.
- Church, J. A., J. S. Godfrey, D. R. Jackett, and T. J. McDougall, 1991: A model of sea level rise caused by ocean thermal expansion. *J. Climate*, **4**, 438–456, [https://doi.org/10.1175/1520-0442\(1991\)004<0438:AMOSLR>2.0.CO;2](https://doi.org/10.1175/1520-0442(1991)004<0438:AMOSLR>2.0.CO;2).
- Couldrey, M. P., and Coauthors, 2021: What causes the spread of model projections of ocean dynamic sea-level change in response to greenhouse gas forcing? *Climate Dyn.*, **56**, 155–187, <https://doi.org/10.1007/s00382-020-05471-4>.
- Dias, F. B., and Coauthors, 2020: Ocean heat storage in response to changing ocean circulation processes. *J. Climate*, **33**, 9065–9082, <https://doi.org/10.1175/JCLI-D-19-1016.1>.
- Dong, Y., C. Proistosescu, K. C. Armour, and D. S. Battisti, 2019: Attributing historical and future evolution of radiative feedbacks to regional warming patterns using a Green's function approach: The preeminence of the western Pacific. *J. Climate*, **32**, 5471–5491, <https://doi.org/10.1175/JCLI-D-18-0843.1>.
- Drijfhout, S., G. J. van Oldenborgh, and A. Cimatoribus, 2012: Is a decline of AMOC causing the warming hole above the North Atlantic in observed and modeled warming patterns? *J. Climate*, **25**, 8373–8379, <https://doi.org/10.1175/JCLI-D-12-00490.1>.
- Dunstan, P. K., and Coauthors, 2018: Global patterns of change and variation in sea surface temperature and chlorophyll *a*. *Sci. Rep.*, **8**, 14624, <https://doi.org/10.1038/s41598-018-33057-y>.
- Eby, M., K. Zickfeld, A. Montenegro, D. Archer, K. J. Meissner, and A. J. Weaver, 2009: Lifetime of anthropogenic climate change: Millennial time scales of potential CO₂ and surface temperature perturbations. *J. Climate*, **22**, 2501–2511, <https://doi.org/10.1175/2008JCLI2554.1>.
- Exarchou, E., T. Kuhlbrodt, J. M. Gregory, and R. S. Smith, 2015: Ocean heat uptake processes: A model intercomparison. *J. Climate*, **28**, 887–908, <https://doi.org/10.1175/JCLI-D-14-00235.1>.
- Feucher, C., G. Maze, and H. Mercier, 2019: Subtropical mode water and permanent pycnocline properties in the World Ocean. *J. Geophys. Res. Oceans*, **124**, 1139–1154, <https://doi.org/10.1029/2018JC014526>.
- Frankcombe, L. M., M. H. England, M. E. Mann, and B. A. Steinman, 2015: Separating internal variability from the externally forced climate response. *J. Climate*, **28**, 8184–8202, <https://doi.org/10.1175/JCLI-D-15-0069.1>.
- Frederikse, T., and Coauthors, 2020: The causes of sea-level rise since 1900. *Nature*, **584**, 393–397, <https://doi.org/10.1038/s41586-020-2591-3>.
- Frölicher, T. L., J. L. Sarmiento, D. J. Paynter, J. P. Dunne, J. P. Krasting, and M. Winton, 2015: Dominance of the Southern Ocean in anthropogenic carbon and heat uptake in CMIP5 models. *J. Climate*, **28**, 862–886, <https://doi.org/10.1175/JCLI-D-14-00117.1>.
- Fukumori, I., T. Lee, B. Cheng, and D. Menemenlis, 2004: The origin, pathway, and destination of Niño-3 water estimated

- by a simulated passive tracer and its adjoint. *J. Phys. Oceanogr.*, **34**, 582–604, <https://doi.org/10.1175/2515.1>.
- Garuba, O. A., and B. A. Klinger, 2016: Ocean heat uptake and interbasin transport of the passive and redistributive components of surface heating. *J. Climate*, **29**, 7507–7527, <https://doi.org/10.1175/JCLI-D-16-0138.1>.
- , and —, 2018: The role of individual surface flux components in the passive and active ocean heat uptake. *J. Climate*, **31**, 6157–6173, <https://doi.org/10.1175/JCLI-D-17-0452.1>.
- Gebbie, G., and P. Huybers, 2019: The Little Ice Age and 20th-century deep Pacific cooling. *Science*, **363**, 70–74, <https://doi.org/10.1126/science>.
- Gnanadesikan, A., 1999: A simple predictive model for the structure of the oceanic pycnocline. *Science*, **283**, 2077–2079, <https://doi.org/10.1126/science.283.5410.2077>.
- Gregory, J. M., 2000: Vertical heat transports in the ocean and their effect on time-dependent climate change. *Climate Dyn.*, **16**, 501–515, <https://doi.org/10.1007/s003820000059>.
- , and Coauthors, 2016: The Flux-Anomaly-Forced Model Intercomparison Project (FAFMIP) contribution to CMIP6: Investigation of sea-level and ocean climate change in response to CO₂ forcing. *Geosci. Model Dev.*, **9**, 3993–4017, <https://doi.org/10.5194/gmd-9-3993-2016>.
- Gruber, N., 2011: Warming up, turning sour, losing breath: Ocean biogeochemistry under global change. *Philos. Trans. Roy. Soc. London*, **A369**, 1980–1996, <https://doi.org/10.1098/rsta.2011.0003>.
- He, C., Z. Liu, and A. Hu, 2019: The transient response of atmospheric and oceanic heat transports to anthropogenic warming. *Nat. Climate Change*, **9**, 222–226, <https://doi.org/10.1038/s41558-018-0387-3>.
- Hu, S., S.-P. Xie, and W. Liu, 2020: Global pattern formation of net ocean surface heat flux response to greenhouse warming. *J. Climate*, **33**, 7503–7522, <https://doi.org/10.1175/JCLI-D-19-0642.1>.
- Huber, M. B., and L. Zanna, 2017: Drivers of uncertainty in simulated ocean circulation and heat uptake. *Geophys. Res. Lett.*, **44**, 1402–1413, <https://doi.org/10.1002/2016GL071587>.
- Jackett, D. R., and T. J. McDougall, 1997: A neutral density variable for the world's oceans. *J. Phys. Oceanogr.*, **27**, 237–263, [https://doi.org/10.1175/1520-0485\(1997\)027<0237:ANDVFT>2.0.CO;2](https://doi.org/10.1175/1520-0485(1997)027<0237:ANDVFT>2.0.CO;2).
- , —, M. H. England, and A. C. Hirst, 2000: Thermal expansion in ocean and coupled general circulation models. *J. Climate*, **13**, 1384–1405, [https://doi.org/10.1175/1520-0442\(2000\)013<1384:TEIOAC>2.0.CO;2](https://doi.org/10.1175/1520-0442(2000)013<1384:TEIOAC>2.0.CO;2).
- Kent, C., R. Chadwick, and D. P. Rowell, 2015: Understanding uncertainties in future projections of seasonal tropical precipitation. *J. Climate*, **28**, 4390–4413, <https://doi.org/10.1175/JCLI-D-14-00613.1>.
- Khatiwala, S., 2007: A computational framework for simulation of biogeochemical tracers in the ocean. *Global Biogeochem. Cycles*, **21**, GB3001, <https://doi.org/10.1029/2007GB002923>.
- , 2018: Transport Matrix Method software for ocean biogeochemical simulations. Zenodo, <https://doi.org/10.5281/zenodo.1246300>.
- , M. Visbeck, and M. Cane, 2005: Accelerated simulation of passive tracers in ocean circulation models. *Ocean Modell.*, **9**, 51–69, <https://doi.org/10.1016/j.ocemod.2004.04.002>.
- , F. Primeau, and M. Holzer, 2012: Ventilation of the deep ocean constrained with tracer observations and implications for radiocarbon estimates of ideal mean age. *Earth Planet. Sci. Lett.*, **325–326**, 116–125, <https://doi.org/10.1016/j.epsl.2012.01.038>.
- , H. D. Graven, S. Payne, and P. Heimbach, 2018: Changes to the air–sea flux and distribution of radiocarbon in the ocean over the 21st century. **45**, 5617–5626, <https://doi.org/10.1029/2018GL078172>.
- , A. Schmittner, and J. Muglia, 2019: Air–sea disequilibrium enhances ocean carbon storage during glacial periods. *Sci. Adv.*, **5**, eaaw4981, <https://doi.org/10.1126/sciadv.aaw4981>.
- Kostov, Y., K. C. Armour, and J. Marshall, 2014: Impact of the Atlantic meridional overturning circulation on ocean heat storage and transient climate change. *Geophys. Res. Lett.*, **41**, 2108–2116, <https://doi.org/10.1002/2013GL058998>.
- Kuhlbrodt, T., and J. M. Gregory, 2012: Ocean heat uptake and its consequences for the magnitude of sea level rise and climate change. *Geophys. Res. Lett.*, **39**, L18608, <https://doi.org/10.1029/2012GL052952>.
- Kvale, K. F., S. Khatiwala, H. Dietze, I. Kriest, and A. Oschlies, 2017: Evaluation of the transport matrix method for simulation of ocean biogeochemical tracers. *Geosci. Model Dev.*, **10**, 2425–2445, <https://doi.org/10.5194/gmd-10-2425-2017>.
- Larson, S. M., D. J. Vimont, A. C. Clement, and B. P. Kirtman, 2018: How momentum coupling affects SST variance and large-scale Pacific climate variability in CESM. *J. Climate*, **31**, 2927–2944, <https://doi.org/10.1175/JCLI-D-17-0645.1>.
- Levitus, S., and Coauthors, 2012: World ocean heat content and thermosteric sea level change (0–2000 m), 1955–2010. *Geophys. Res. Lett.*, **39**, L10603, <https://doi.org/10.1029/2012GL051106>.
- Li, Q., Y. Luo, and F. Liu, 2019: Response of the subtropical gyre circulation in the North Pacific Ocean to CO₂ quadrupling. *Atmos.–Ocean*, **57**, 307–317, <https://doi.org/10.1080/07055900.2019.1666701>.
- Lowe, J. A., and J. M. Gregory, 2006: Understanding projections of sea level rise in a Hadley Centre coupled climate model. *J. Geophys. Res.*, **111**, C11014, <https://doi.org/10.1029/2005JC003421>.
- Luo, Y., J. Lu, F. Liu, and W. Liu, 2015: Understanding the El Niño-like oceanic response in the tropical Pacific to global warming. *Climate Dyn.*, 1945–1964, <https://doi.org/10.1007/s00382-014-2448-2>.
- , —, —, and O. Garuba, 2017: The role of ocean dynamical thermostat in delaying the El Niño-like response over the equatorial Pacific to climate warming. *J. Climate*, **30**, 2811–2827, <https://doi.org/10.1175/JCLI-D-16-0454.1>.
- Luyten, J. R., J. Pedlosky, and H. Stommel, 1983: The ventilated thermocline. *J. Phys. Oceanogr.*, **13**, 292–309, [https://doi.org/10.1175/1520-0485\(1983\)013<0292:TVT>2.0.CO;2](https://doi.org/10.1175/1520-0485(1983)013<0292:TVT>2.0.CO;2).
- Lyman, J. M., and G. C. Johnson, 2014: Estimating global ocean heat content changes in the upper 1800 m since 1950 and the influence of climatology choice. *J. Climate*, **27**, 1945–1957, <https://doi.org/10.1175/JCLI-D-12-00752.1>.
- Lyu, K., X. Zhang, and J. A. Church, 2021: Projected ocean warming constrained by the ocean observational record. *Nat. Climate Change*, **11**, 834–839, <https://doi.org/10.1038/s41558-021-01151-1>.
- Ma, J., and S.-P. Xie, 2013: Regional patterns of sea surface temperature change: A source of uncertainty in future projections of precipitation and atmospheric circulation. *J. Climate*, **26**, 2482–2501, <https://doi.org/10.1175/JCLI-D-12-00283.1>.
- Ma, X., and Coauthors, 2016: Western boundary currents regulated by interaction between ocean eddies and the

- atmosphere. *Nature*, **535**, 533–537, <https://doi.org/10.1038/nature18640>.
- , W. Liu, R. J. Allen, G. Huang, and X. Li, 2020: Dependence of regional ocean heat uptake on anthropogenic warming scenarios. *Sci. Adv.*, **6**, eabc0303, <https://doi.org/10.1126/sciadv.abc0303>.
- Marshall, D. P., and L. Zanna, 2014: A conceptual model of ocean heat uptake under climate change. *J. Climate*, **27**, 8444–8465, <https://doi.org/10.1175/JCLI-D-13-00344.1>.
- Marshall, J., and K. Speer, 2012: Closure of the meridional overturning circulation through Southern Ocean upwelling. *Nat. Geosci.*, **5**, 171–180, <https://doi.org/10.1038/ngeo1391>.
- , J. R. Scott, K. C. Armour, J. M. Campin, M. Kelley, and A. Romanou, 2015: The ocean's role in the transient response of climate to abrupt greenhouse gas forcing. *Climate Dyn.*, **44**, 2287–2299, <https://doi.org/10.1007/s00382-014-2308-0>.
- , —, A. Romanou, M. Kelley, and A. Leboissetier, 2017: The dependence of the ocean's MOC on mesoscale eddy diffusivities: A model study. *Ocean Modell.*, **111**, 1–8, <https://doi.org/10.1016/j.ocemod.2017.01.001>.
- Menary, M. B., and R. A. Wood, 2018: An anatomy of the projected North Atlantic warming hole in CMIP5 models. *Climate Dyn.*, **50**, 3063–3080, <https://doi.org/10.1007/s00382-017-3793-8>.
- Meyssignac, B., and Coauthors, 2019: Measuring global ocean heat content to estimate the Earth energy imbalance. *Front. Mar. Sci.*, **6**, 432, <https://doi.org/10.3389/fmars.2019.00432>.
- Morrison, A. K., O. A. Saenko, A. M. Hogg, and P. Spence, 2013: The role of vertical eddy flux in Southern Ocean heat uptake. *Geophys. Res. Lett.*, **40**, 5445–5450, <https://doi.org/10.1002/2013GL057706>.
- Muglia, J., L. C. Skinner, and A. Schmittner, 2018: Weak overturning circulation and high Southern Ocean nutrient utilization maximized glacial ocean carbon. *Earth Planet. Sci. Lett.*, **496**, 47–56, <https://doi.org/10.1016/j.epsl.2018.05.038>.
- Newsom, E., L. Zanna, S. Khatiwala, and J. M. Gregory, 2020: The influence of warming patterns on passive ocean heat uptake. *Geophys. Res. Lett.*, **47**, e2020GL088429, <https://doi.org/10.1029/2020GL088429>.
- Nie, X., S. Gao, F. Wang, J. Chi, and T. Qu, 2019: Origins and pathways of the Pacific equatorial undercurrent identified by a simulated adjoint tracer. *J. Geophys. Res. Oceans*, **124**, 2331–2347, <https://doi.org/10.1029/2018JC014212>.
- Nikurashin, M., and G. Vallis, 2012: A theory of the interhemispheric meridional overturning circulation and associated stratification. *J. Phys. Oceanogr.*, **42**, 1652–1667, <https://doi.org/10.1175/JPO-D-11-0189.1>.
- Palmer, M. D., and K. Haines, 2009: Estimating oceanic heat content change using isotherms. *J. Climate*, **22**, 4953–4969, <https://doi.org/10.1175/2009JCLI2823.1>.
- , and Coauthors, 2017: Ocean heat content variability and change in an ensemble of ocean reanalyses. *Climate Dyn.*, **49**, 909–930, <https://doi.org/10.1007/s00382-015-2801-0>.
- Pardaens, A. K., J. A. Lowe, S. Brown, R. J. Nicholls, and D. de Gusmão, 2011: Sea-level rise and impacts projections under a future scenario with large greenhouse gas emission reductions. *Geophys. Res. Lett.*, **38**, L12604, <https://doi.org/10.1029/2011GL047678>.
- Purkey, S. G., G. C. Johnson, L. D. Talley, B. M. Sloyan, S. E. Wijffels, W. Smethie, S. Mecking, and K. Katsumata, 2019: Unabated bottom water warming and freshening in the South Pacific Ocean. *J. Geophys. Res. Oceans*, **124**, 1778–1794, <https://doi.org/10.1029/2018JC014775>.
- Qu, T., S. Gao, I. Fukumori, R. A. Fine, and E. J. Lindstrom, 2009: Origin and pathway of equatorial 13°C water in the Pacific identified by a simulated passive tracer and its adjoint. *J. Phys. Oceanogr.*, **39**, 1836–1853, <https://doi.org/10.1175/2009JPO4045.1>.
- , —, and R. A. Fine, 2013: Subduction of South Pacific tropical water and its equatorward pathways as shown by a simulated passive tracer. *J. Phys. Oceanogr.*, **43**, 1551–1565, <https://doi.org/10.1175/JPO-D-12-0180.1>.
- Roemmich, D., J. Church, J. Gilson, D. Monselesan, P. Sutton, and S. Wijffels, 2015: Unabated planetary warming and its ocean structure since 2006. *Nat. Climate Change*, **5**, 240–245, <https://doi.org/10.1038/nclimate2513>.
- Rugenstein, M., M. Winton, R. J. Stouffer, S. M. Griffies, and R. Hallberg, 2013: Northern high-latitude heat budget decomposition and transient warming. *J. Climate*, **26**, 609–621, <https://doi.org/10.1175/JCLI-D-11-00695.1>.
- Saenko, O. A., D. Yang, and J. M. Gregory, 2018: Impact of mesoscale eddy transfer on heat uptake in an eddy-parameterizing ocean model. *J. Climate*, **31**, 8589–8606, <https://doi.org/10.1175/JCLI-D-18-0186.1>.
- , J. M. Gregory, S. M. Griffies, M. P. Couldrey, and F. B. Dias, 2021: Contribution of ocean physics and dynamics at different scales to heat uptake in low-resolution AOGCMs. *J. Climate*, **34**, 2017–2035, <https://doi.org/10.1175/JCLI-D-20-0652.1>.
- Shi, J. R., S. P. Xie, and L. D. Talley, 2018: Evolving relative importance of the Southern Ocean and North Atlantic in anthropogenic ocean heat uptake. *J. Climate*, **31**, 7459–7479, <https://doi.org/10.1175/JCLI-D-18-0170.1>.
- Sun, S., 2020: Transient overturning compensation between Atlantic and Indo-Pacific basins. *J. Phys. Oceanogr.*, **50**, 2151–2172, <https://doi.org/10.1175/JPO-D-20-0060.1>.
- Tesdal, J. E., and R. P. Abernathy, 2021: Drivers of local ocean heat content variability in ECCOv4. *J. Climate*, **34**, 2941–2956, <https://doi.org/10.1175/JCLI-D-20-0058.1>.
- Todd, A., and Coauthors, 2020: Ocean-only FAFMIP: Understanding regional patterns of ocean heat content and dynamic sea level change. *J. Adv. Model. Earth Syst.*, **12**, e2019MS002027, <https://doi.org/10.1029/2019MS002027>.
- Wang, G., S. P. Xie, R. X. Huang, and C. Chen, 2015: Robust warming pattern of global subtropical oceans and its mechanism. *J. Climate*, **28**, 8574–8584, <https://doi.org/10.1175/JCLI-D-14-00809.1>.
- , L. Cheng, J. Abraham, and C. Li, 2018: Consensuses and discrepancies of basin-scale ocean heat content changes in different ocean analyses. *Climate Dyn.*, **50**, 2471–2487, <https://doi.org/10.1007/s00382-017-3751-5>.
- Weaver, A. J., and Coauthors, 2001: The UVic Earth system climate model: Model description, climatology, and applications to past, present and future climates. *Atmos.–Ocean*, **39**, 361–428, <https://doi.org/10.1080/07055900.2001.9649686>.
- Williams, R. G., A. Katavouta, and V. Roussenov, 2021: Regional asymmetries in ocean heat and carbon storage due to dynamic redistribution in climate model projections. *J. Climate*, **34**, 3907–3925, <https://doi.org/10.1175/JCLI-D-20-0519.1>.
- Winton, M., S. M. Griffies, B. L. Samuels, J. L. Sarmiento, and T. L. Frölicher, 2013: Connecting changing ocean circulation with changing climate. *J. Climate*, **26**, 2268–2278, <https://doi.org/10.1175/JCLI-D-12-00296.1>.
- Xie, P., and G. K. Vallis, 2012: The passive and active nature of ocean heat uptake in idealized climate change experiments.

- Climate Dyn.*, **38**, 667–684, <https://doi.org/10.1007/s00382-011-1063-8>.
- Xie, S., 2020: Ocean warming pattern effect on global and regional climate change. *AGU Adv.*, **1**, e2019AV000130, <https://doi.org/10.1029/2019AV000130>.
- Yang, H., and Coauthors, 2020: Poleward shift of the major ocean gyres detected in a warming climate. *Geophys. Res. Lett.*, **47**, e2019GL085868, <https://doi.org/10.1029/2019GL085868>.
- Zanna, L., S. Khatiwala, J. M. Gregory, J. Ison, and P. Heimbach, 2019: Global reconstruction of historical ocean heat storage and transport. *Proc. Natl. Acad. Sci. USA*, **116**, 1126–1131, <https://doi.org/10.1073/pnas.1808838115>.
- Zhai, X., H. L. Johnson, and D. P. Marshall, 2014: A simple model of the response of the Atlantic to the North Atlantic Oscillation. *J. Climate*, **27**, 4052–4069, <https://doi.org/10.1175/JCLI-D-13-00330.1>.
- Zheng, X. T., S. P. Xie, L. H. Lv, and Z. Q. Zhou, 2016: Intermodel uncertainty in ENSO amplitude change tied to Pacific Ocean warming pattern. *J. Climate*, **29**, 7265–7279, <https://doi.org/10.1175/JCLI-D-16-0039.1>.
- Zika, J. D., J. M. Gregory, E. L. McDonagh, A. Marzocchi, and L. Clément, 2021: Recent water mass changes reveal mechanisms of ocean warming. *J. Climate*, **34**, 3461–3479, <https://doi.org/10.1175/JCLI-D-20-0355.1>.